INVESTIGATION OF VARIABLE STIFFNESS BASED POLYMER MORPHING STRUCTURES

by

Eliot Zbozny George

B.S. in Mechanical Engineering, University of Pittsburgh, 2008

Submitted to the Graduate Faculty of

the Swanson School of Engineering in partial fulfillment

of the requirements for the degree of

Master of Science in Mechanical Engineering

University of Pittsburgh

2015

UNIVERSITY OF PITTSBURGH

SWANSON SCHOOL OF ENGINEERING

This thesis was presented

by

Eliot Zbozny George

It was defended on

April 20th, 2015

and approved by

William S. Slaughter, Ph.D., Associate Professor,
Department of Mechanical Engineering and Materials Science

John C. Brigham, Ph.D., Assistant Professor
Department of Civil and Environmental Engineering

Thesis Advisor: William W. Clark, Ph.D., Professor
Department of Mechanical Engineering and Materials Science

INVESTIGATION OF VARIABLE STIFFNESS BASED POLYMER MORPHING STRUCTURES

Eliot Zbozny George, M.S.

University of Pittsburgh, 2015

Morphing structures have a multitude of potential applications in many engineering fields. Control surfaces for aircraft, pumps and valves for artificial organs or any application where a complex motion is required and can benefit from incorporating a morphing structure. The ability of a morphing structure to change its shape or configuration can potentially allow designs and functionality that would be impossible to realize without morphing. The focus of this thesis is to investigate the feasibility and operation of a structural shape morphing structure. Structural shape morphing is defined as shape change through material modulus changes. This allows fewer actuators, fewer moving parts and lower energy consumption to effect the same change in configuration as a traditional shape change structure. The morphing structure examined was designed and created specifically for this work and is composed almost entirely of polymer materials. The design utilizes electrical voltage to control the structural stiffness and motion of the structure independently. A review of literature covering fabrication and modeling in morphing structures, polymer actuators, variable modulus materials and variable stiffness structures is presented. A conceptual design for a shape morphing structure is fabricated and refined and an analytical model is developed for the structure to predict its response to applied voltages. The morphing structure's capabilities are measured through experimental testing and the predictions of the analytical model are compared to the results. We demonstrate shape morphing by deforming the structure with an actuator, increasing the effective structural

modulus and then removing the actuation force. Our tests show a fixed shape change in the structure of up to 20% of the total deformation. Feasibility is also discussed for real-world applications and suggested areas for further exploration on the topic are presented.

TABLE OF CONTENTS

LIST OF TABLES

LIST OF FIGURES

ACKNOWLEDGEMENTS

First and foremost, a huge debt of gratitude is due to Dr. William “Buddy” Clark. This work would not be possible without his support and guidance.

I would also like to thank everyone else in the Ionomer and hydrogel variable modulus material collaboration for their expertise and insight; Dr. Tara Meyer, Dr. David Swigon, Dr. Anna Vainchtein, Dr. Haitao Liu, Jeff Auletta, Colin Ladd and Hang Nguyen.

Thanks to all my lab mates for their help and friendship and last but not least, I would like to thank my friends and family for their constant support.

1.0 INTRODUCTION

In many engineering applications, structures or their components must change shape to one or more other configurations. Traditionally, this is accomplished with a number of kinematic joints or elastic/plastic deformation of elements within the structure itself to permit motion of components relative to one another, a means of actuation to move the components and a form of lock to keep the structure in the desired shape if the actuation force is to be removed. This traditional arrangement corresponds to shape change (Motlagh, 2013). This work however focuses on a category of shape changing structures utilizing variable modulus to allow shape change and fix the structure in the desired configuration with lower actuation energy requirements. Figure 1-1 shows a simplified one degree of freedom shape morphing structure with a parallel actuator and variable modulus structure in the four stages of shape morphing. From Figure 1-1, we can also define the two distance measurements "Displacement" and "Hold" to describe the motion and shape change in the structure.

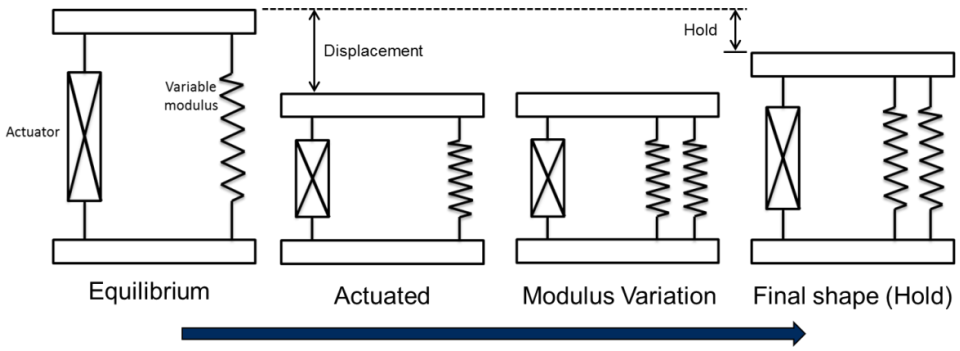

Figure 1-1: Diagram of simplified shape morphing structure in the four stages of shape morphing

This arrangement corresponds to shape morphing (Motlagh, 2013). Most shape morphing research has focused on the use of shape memory materials, either alloys (SMA) or polymers (SMP). While it can be argued that they represent a shape morphing structure, as they combine both variable modulus and the actuation force, they only have several potential positions and it is impossible to separate the change in modulus from applied forces. The focus of this thesis is to explore a novel design for a polymer shape morphing structure utilizing separate actuation and variable modulus components. The actuation force is supplied by a type of dielectric electroactive polymer (DEAP) and the variable modulus structure is composed of a special electroactive polymer utilizing the Johnsen-Rahbek effect. Both the actuator and variable modulus structure are controllable via electric potential and allow change of the structure's shape.

A comprehensive literature review on the existing shape morphing methods and numerical analysis, DEAP fabrication and modeling, and variable modulus structures is presented. Analytical and numerical methods are used to create a model for the response of the structure which is then compared to measured system response. Suggestions for future work in the area are also given.

2.0 LITERATURE REVIEW

2.1 SHAPE MORPHING

Following the distinction between shape change and shape morphing as defined by Motlagh (Motlagh, 2013) and outline graphically in Figure 2-1, this work focuses on shape morphing, or morphing by variation of modulus.

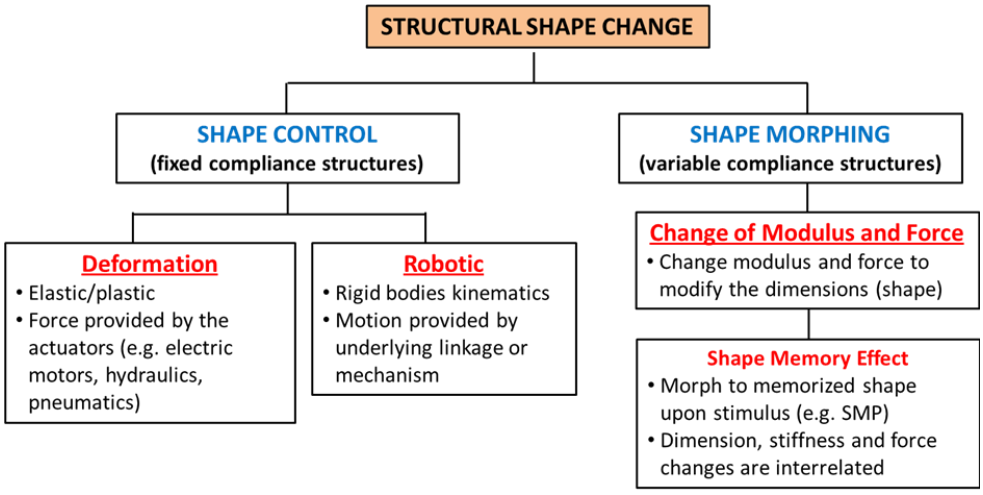

Figure 2-1: Categories of shape control and shape morphing methods (Motlagh, 2013)

The work by Motlagh contains a thorough review of both shape change and shape morphing methods, since shape change is not used in this work, it will not be reviewed here. Anyone interested in the current state of the art of shape change should review Motlagh's work. The focus of Motlagh's work though, is the development of a computational framework for

shape morphing simulation and control. In the work, the problem of forward (morphing change by varied modulus, under constant load and boundary conditions) and inverse (morphing the structure to a selected arbitrary shape by variation of modulus and loading) morphing are defined and modeled. The model developed by Motlagh does not focus on a particular means of actuation or variable modulus structure, allowing it to be applied to potentially any shape morphing structure due to its generality and completeness.

Another study into shape morphing computation by Wang and Brigham (Wang and Brigham, 2012) focused on the use of thermally activated shape memory polymers (SMP) as the variable modulus structure in a smart structural link and a structural backbone. The smart link is essentially a joint that allows other parts of the structure to change positions relative to one another by morphing and is coupled to the structure at the end points. The structural backbone acts to control the shape of a portion or all of the structure through morphing by being directly coupled over the entire backbone rather than just at the end points. Simulation and optimization of a control strategy for both the forward and inverse problems are presented. As a thermal SMP is the focus, temperature distribution and the coupled thermo-mechanical model are simulated.

Shape morphing using SMP was explored by Rauscher (Rauscher, 2008) to create morphing tiles for use in aircraft wings. The SMP used was thermally activated, softening from a rigid state when electric current was passed through embedded heaters. Once softened, the tile demonstrated the ability to shear in plane via external forces, and become rigid once heat was removed. Upon heating again, the tile returned to its original un-sheared state without external forces via the shape memory effect.

2.2 DIELECTRIC ELECTROACTIVE POLYMERS

Though dielectric electroactive polymers (DEAP) are termed “electroactive”, “electrostrictive” is more accurate as the polymers used in their fabrication have no special electronic properties other than being dielectrics. Semantics aside, electroactive is the most commonly used term to describe them in current literature so this work will follow that convention. In the most basic form, an actuator utilizing a DEAP is comprised of the polymer in the form of a thin sheet, in a round, square or other arbitrary planar shape, and two thin electrodes of similar shape and size that are compliant to a similar degree in the areal plane as the polymer without sustaining physical damage or losing conductivity. When an electric potential is applied across the electrodes, the resulting electric field and thus, the induced electrostatic pressure or Maxwell stress causes a compressive strain in the thickness direction of the polymer. As the polymers used are close to incompressible, the area of the sheet must expand to counteract the contraction in the thickness direction. This areal expansion is harnessed in DEAP actuators to apply force. A diagram of this actuation process is shown in Figure 2-2. The previous decade has seen a lot of excitement and research work in the field of DEAP actuators, sensors and power harvesting units but few applications have been brought to market.

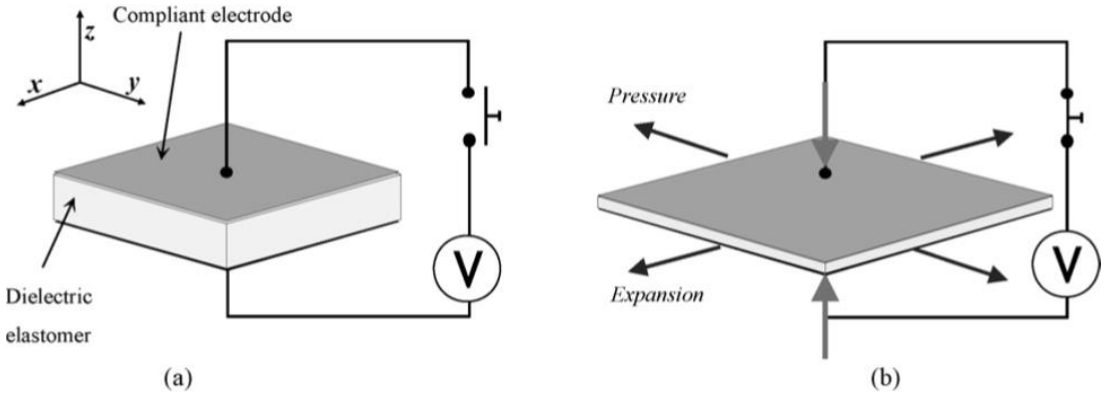

Figure 2-2: Diagram of DEAP actuation principle (Jung et al., 2007)

2.2.1 Actuator design and fabrication.

Since it's not possible for every form of a DEAP actuator that has been explored in prior research to be outlined here, focus is placed on some of the more innovative concepts in the current state of the art.

Shian (Shian et al., 2013) has demonstrated a tunable optical lens based on a clear DEAP diaphragm actuator, a passive clear elastomer diaphragm and a clear fluid trapped between them to couple their deformations hydrostatically. The clear actuator is fabricated by using a clear elastomer (3M VHB) and single walled carbon nanotube (SWCNT) mats for the clear electrodes. The diaphragms are constrained at their edges in a frame and the actuation of the DEAP diaphragm allows the passive diaphragm to flatten and the DEAP to bow outward. This causes a change in focal length proportional to the voltage applied to the DEAP. The lens has a response of less than a second and is capable of focal length changes of over 100% depending on the initial focal length with optical transmittance of 88% at the 550nm wavelength. Images taken by a CMOS detector through the lens at a variety of focal lengths are shown in Figure 2-3 and illustrate the lens's capability.

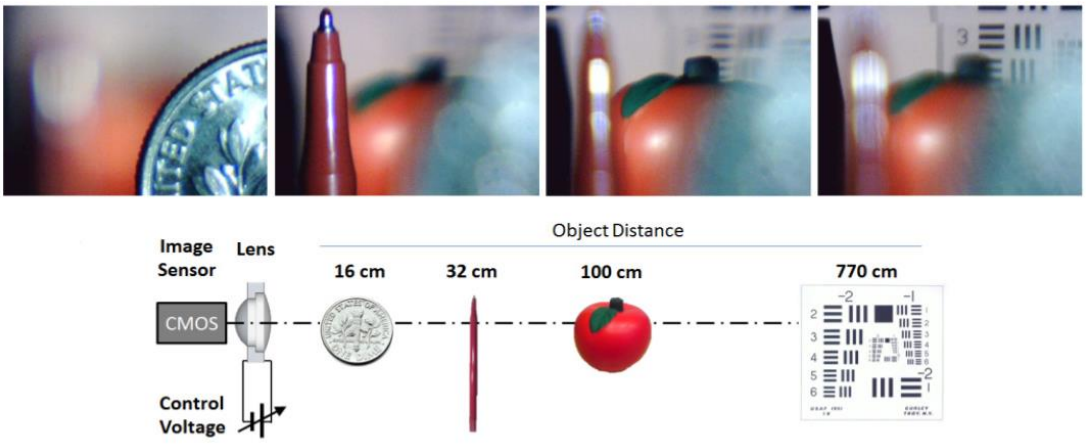

Figure 2-3: Demonstration of tunable DEAP lens capability (Shian et al., 2013)

Usually in conventional motion control applications, a form of displacement sensor is employed to allow closed-loop control. Using the similarity of a DEAP to a parallel plate capacitor, Jung (Jung et al., 2007) demonstrated the ability to measure the change in thickness of the polymer during actuation. The measurement of the capacitance between the electrodes and thus their separation while simultaneously applying high voltage for actuation is accomplished by employing a low frequency voltage (close to constant) for actuation and higher frequency (100hz) voltage signal for measurement sensing. The output sensing signal can then be extracted by using the frequency difference to separate the signal into the actuation voltage and sensing voltage components. While not a direct measurement of the displacement of the actuator, it should be possible to allow closed loop control of an actuator or morphing structure without a separate measurement device if a robust and accurate model of the actuator and attached structure is employed.

In order to increase the output force a DEAP actuator produces, multiple DEAP layers are typically combined into a single structure with all of the individual positive and negative electrodes interconnected in parallel. Fabrication of thin (<100um) polymer elastomer layers coated with conformal compliant electrodes is a challenge in itself. Producing five or six such actuator layers and coupling them together becomes extremely difficult. The high voltages used in actuation (2-4kv) allow any point of weakness in the actuator due to airborne particles, non-uniform elastomer or electrode thickness to suffer a dielectric break down and short circuit. These potential areas of weakness are illustrated in Figure 2-4.

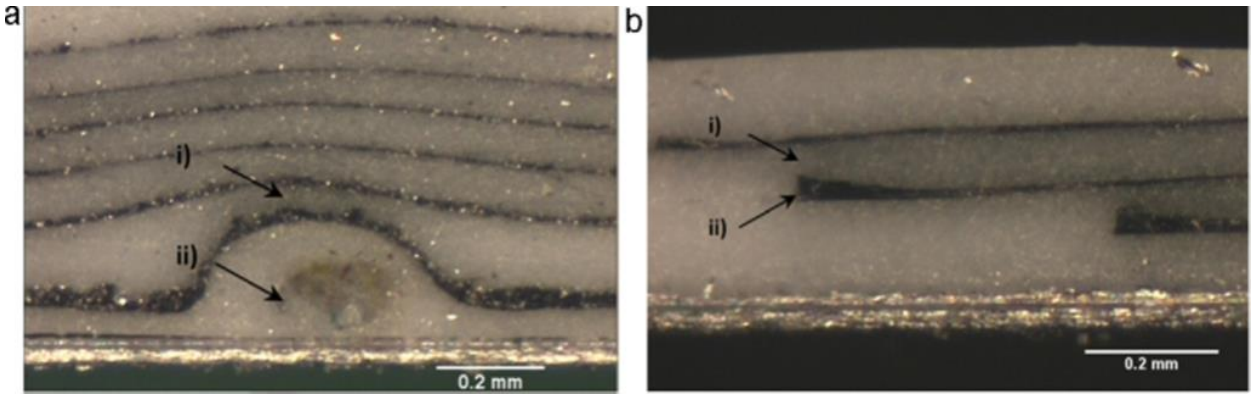

Figure 2-4: Cross section through multi-layer actuators highlighting areas of weakness; (a) area of weakness (i) due to airborne particle inclusion (ii), (b) Area of weakness (i) due to non-uniform electrode thickness (ii) (Araromi et al., 2011)

Araromi (Araromi et al., 2011) has detailed a method in which multi-layer silicone and graphite actuators are fabricated by thinning the elastomer and electrode material viscosity and spray depositing them sequentially on moving substrates. In this manner, they have produced functional actuators of up to six coupled DEAP layers with good film thickness uniformity.

An area of actuator design and fabrication that poses a constant challenge is the choice and application method of the electrode material. The requirement of large strain capability without generating significant opposing forces, all while maintaining electrical conductivity is a difficult group of material parameters to meet. A comprehensive examination of different electrode materials was produced by Akbey (Akbey, 2004) and is an excellent resource for electrode selection in the design of DEAP actuators. Actuators usually have one of the following categories of electrode; grease, rubber or metal. In the grease category, conductive powder is applied by brushing or solvent (usually Heptane) carrier spray deposition of conductive particles suspended in a polymer carrier, typically a high viscosity fluid at room temperature are the main methods. The conductive particles in both groups are typically silver or carbon and the polymer

carrier in the grease family can be a silicone grease or similar viscosity fluid. In the rubber group, the same conductive particle powders are suspended in a polymer carrier that sets i.e. silicone elastomer. Typically in the research setting, both the grease and rubber (before setting) families are brushed on manually with the addition of a solvent, usually Heptane again, to adjust the viscosity to permit application of a film with a uniform thickness.

The final group, metals are generally more difficult to design with, as they are typically not nearly as compliant as the elastomer layers. Despite this, sputtered or evaporated metallic electrodes have been used by patterning the electrode to allow expansion without cracking by Kornbluh (Kornbluh et al, 1999) or by designing the surface topology to accommodate the strains by Benslimane (Benslimane et at., 2002). These two solutions for metallic electrode designs are detailed in Figure 2-5. One of the few commercially available DEAP actuators, produced by Danfoss Poly-Power, is of the sinusoidal surface type. Existing large area thin film coating techniques for metallization have allowed this design to be produced on a commercially viable scale (Hamann and Poole, 2012). Unfortunately, at the time of this work, it appears the Danfoss group has closed the poly-power division despite demonstrating some innovative applications for their DEAP structures.

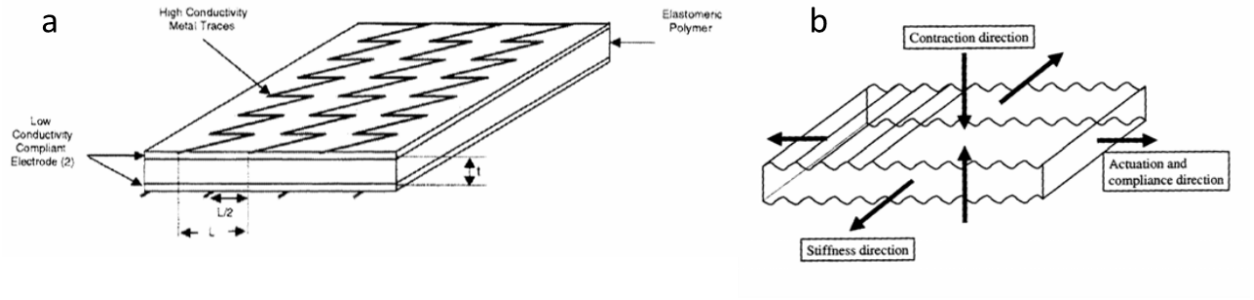

Figure 2-5: Designs for metallic electrodes; (a) zig-zag patterned gold electrodes (Kornbluh et al., 1999), (b) Sinusoidal surface topology with silver electrodes (Benslimane et al., 2002)

Another design for a metallic electrode DEAP is detailed by Wissman (Wissman et al. 2014) using eutectic gallium-indium (EGaIn) electrodes that remain in the liquid phase at room temperature. A uniform electrode layer is applied manually by blotting the liquid through a stencil pattern and applying a seal layer of elastomer to protect and encapsulate it. The actuators used in the Wissman work are of a unique design and composed of poly(dimethylsiloxane) (PDMS) elastomer and the EGaIn electrodes. Essentially free standing, the actuators act as cantilever beams that are in a bent state at rest and straighten when actuated.

Other methods for applying EGaIn and other room temperature liquid phase metals is explored by Lu (Lu et al., 2014) for use in soft electronics and flexible circuit conductors. The use of a CO2 laser to pattern the liquid metal layer directly after application to the elastomer substrate negates the need for the stencils, jet printing or other deposition methods usually used.

2.2.2 Analytical modeling of DEAP actuators.

The challenges of modelling response of the DEAP structure is compounded by the coupling of electric and mechanical behaviors and the highly non-linear materials present in these actuators. The material chosen for the DEAP used in this and many other works, (3M VHB) behaves as a viscoelastic solid which increases the necessary complexity of any accurate model.

Likely the most complete treatment of the material modeling for DEAP actuators, particularly those using acrylic VHB elastomers is the work by Wissler (Wissler, 2014). Wissler has performed the necessary relaxation experiments, built refined viscoelastic models for VHB materials in the Yeoh, Ogden and Aruda-Boyce formulations and validated resulting models with

further experimental material tests. Wissler's work was instrumental in the development of the models used in this work.

The modeling of a diaphragm-type DEAP actuator has been approached several different ways in previous works. Rizzello (Rizzello et al., 2013) modeled a diaphragm actuator as a spring-damper system using a dynamic systems approach. The diaphragm was coupled to a spring and mass to act as a mechanical bias and the resulting dynamic model was used to predict position. The model was then validated experimentally for a range of masses and driving frequencies, however it was found to not be particularly accurate.

Hodgins (Hodgins et al., 2014) approached a similar problem using a viscoelastic free energy model combined with a similar spring-damper dynamics model as Rizzello. The validation of the model showed close approximation to the actuators dynamic and viscoelastic responses. A mass-spring biased DEAP actuator system used in the work by Rizzello is shown in Figure 2-6. The system used in the work by Hodgins is similar.

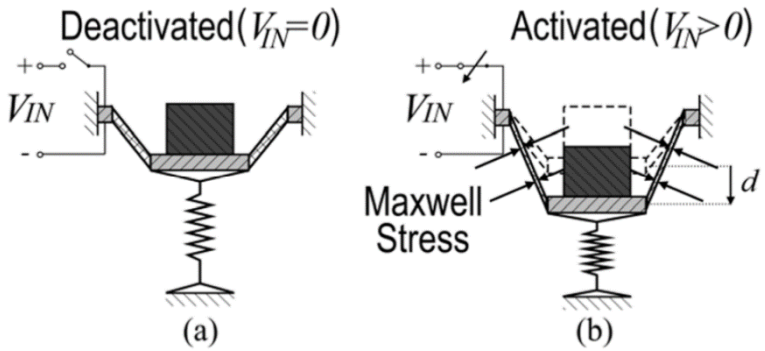

Figure 2-6: Mass-spring biased diaphragm DEAP actuator; (a) unactuated state, (b) actuated state, (Rizzello et al., 2013)

2.3 VARIABLE MODULUS STRUCTURES

Variable modulus structures with potential use in shape morphing structures can be grouped into three categories: shape memory polymers, phase change materials and fluid pressure based structures and finally, electroactive materials.

2.3.1 Shape memory polymers.

Arguably most shape morphing research work to date has utilized shape memory polymers (SMP) for the variable modulus component of the structure. The ability of the materials to undergo large changes in modulus with the application of stimulus, sustain large strains while in the low modulus state, return to the high modulus state, hold the induced shape and recover to the original shape with the reapplication of stimulus makes them well suited for many morphing structures. A graphical representation of a thermal and mechanical loading cycle for a thermally activated SMP is shown in Figure 2-7. While SMP materials can change modulus, there is also an inherent application of force to the structure in their recovery stage. This precludes them from use in structures adhering to the most strict definition of shape morphing. Despite this, they still may have significant potential for shape morphing applications.

Mather (Mather et al., 2009) presents a comprehensive review of SMP materials, research and applications. While most morphing work has focused on thermally activated SMPs, magnetic and light activated materials are being explored in the medical field. The absence of high heat requirements in these materials could be a benefit in certain structural morphing applications.

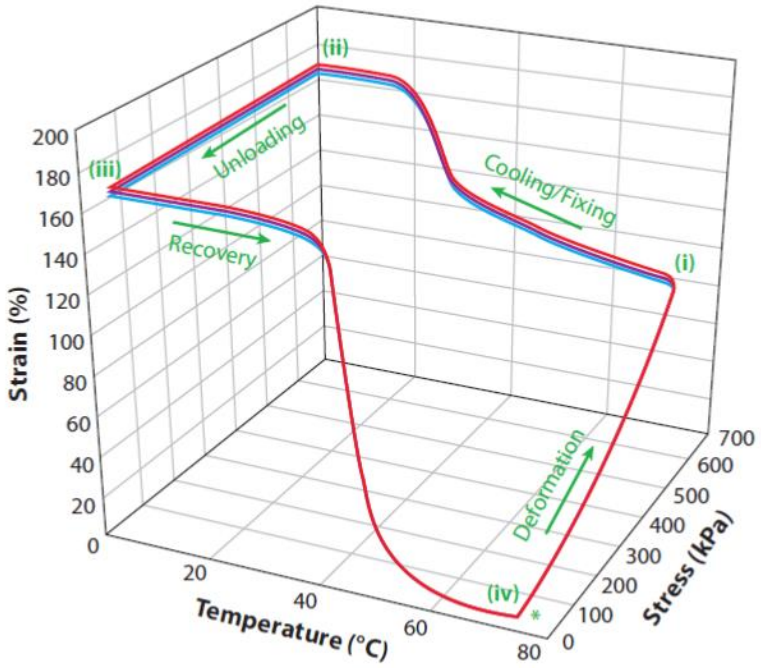

Figure 2-7: Diagram of a thermomechanical cycle for a shape memory polymer (Mather, 2009)

Previously mentioned in the shape morphing section, the work by Rauscher explored the use of tiles constructed of a thermally activated SMP (trade name: Veriflex®) with embedded Ni-chrome heating wires for morphing aircraft wing applications. The resulting tiles were shown to sustain large, recoverable planar shear strains with minimal out of plane buckling deformation due to shearing and aerodynamic loading.

Work by Gross (Gross, 2008) also focused on Veriflex, however in general mechanical properties testing rather than morphing applications specifically. Gross performed tensile, three-point bending and creep testing along with heat transfer rate experiments. From his test data, Gross was able to determine the mechanical properties for hot and cold states of Veriflex shown in Table 2-1.

Table 2-1: Mechanical properties with 95% confidence interval of Veriflex in cold and hot states, (Gross, 2008)

	Cold State Tensile Test	Hot State Tensile Test
Young's Modulus MPa	1010 +/- 58	2.63 +/- 1.20
Tensile Strength MPa	20 +/- 2.69	0.61 +/- 0.08
Tensile Ultimate Strength MPa	19 +/- 2.46	N/A
	Cold State 3 Point Bend Test	Hot State 3 Point Bend Test
Flexural Modulus MPa	700 +/- 37	6.84 +/- 1.71
Flexural Strength MPa	37 +/- 2	0.23 +/- 0.03
Flexural Yield Strength MPa	N/A	N/A

Murray and Gandhi (Murray and Gandhi, 2009) explored multi-layer beams utilizing a thermal SMP to act as shearing layers between stiffer base and cover layers through the creation of a model comparing strain energy and stiffness ratio. A diagram of their concept is shown in Figure 2-8. Also taken into consideration in their model is the energy required in the form of heat to change the state of the SMP layers.

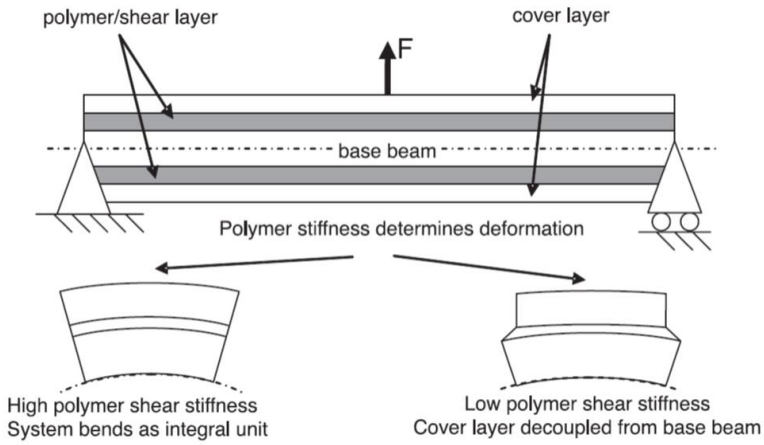

Figure 2-8: Diagram of variable stiffness beam concept employing SMP layers, (Murray and Gandhi, 2009)

Though purely theoretical, the concept by Murray and Gandhi does point to alternate ways to use SMP materials to achieve variable stiffness structures through composite designs rather than a homogenous SMP structure. Since it is only the SMP layers that are changing modulus, we define the change in stiffness as the change in effective structural modulus of the beam rather than as simply a change in modulus. This is to differentiate between the ability of a material to change its material properties such as modulus and the ability of a structure to change its stiffness or effective modulus.

Work by Chen (Chen et al., 2012) describes the use of thermal SMPs to create a multi-layered fiber reinforced composite tube capable of large changes in stiffness between the hot and cold states. Also presented is a model taking the fiber amount and winding angle in the tube into account and predicting the resulting hot and cold state mechanical properties of the tube.

2.3.2 Phase change and fluid pressure structures

As a somewhat odd area in variable stiffness structures, phase change materials haven't seen much research in functional structures. However, their simplicity dictates potential applications where they will are ideally suited. A work by Shan (Shan et al., 2013) demonstrates the use of a low melting temperature alloy encapsulated in a flexible elastomer. When current is passed through the alloy, joule heating causes it to change from a solid to a liquid state. The structure is then flexible and can be easily deformed. Upon the removal of current, heat dissipates and the alloy solidifies in the new shape and the structure becomes rigid.

Another area of variable stiffness structures relying on variation of fluid pressure in channels within the structure to vary rigidity. A work by Philen (Philen, 2010) describes these so-called fluidic flexible matrix composites (F^2MC) systems and develops a comprehensive

system model. In the work, Philen uses a fixed volume of fluid contained in a flexible tube with a control valve and accumulator or fluid supply at one end. With the valve closed, the fluid is trapped and the tube is in a rigid state. Once the valve is open, the tube can deform as the fluid can travel into the accumulator. Philen is able to achieve several orders of magnitude change in stiffness with this method.

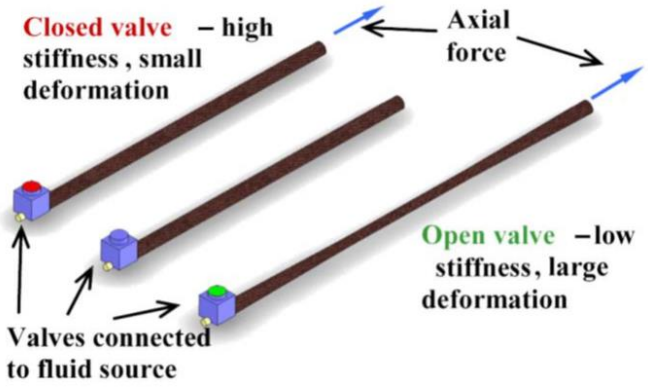

Figure 2-9: F^{2}MC system diagram (Philen, 2010)

2.3.3 Electroactive structures

Variable stiffness structures based on electroactive materials represent a relatively new area of research for morphing applications. Rather than cope with response time, heat transfer and dissipation as in the thermal SMP based materials, electroactive materials allow fast, reversible stiffness changes with little loss of energy in the form of heat.

One type of electroactive material is the Electroplastic elastomer hydrogels (EPEHs) explored by Calvo-Marzal (Calvo-Marzal et al., 2011). These materials change modulus through control of the cross-link density in the polymer. This is manifested by the use of electric potential to reversibly control the reduction-oxidation reaction in the polymer. Transition of the iron

(Fe^{2+}/Fe^{3+}) redox couple controls the cross-link density in the material. The oxidized state, (Fe^{2+}), corresponds with the lower density of cross-linking or soft state of the material while the reduced state, (Fe^{3+}), corresponds with the higher density of cross-linking or rigid state.

A new type of variable stiffness structure is used in this work. It relies on a flexible electroactive polymer, particularly an Ionomer material in a certain structural arrangement to allow variation of the structures stiffness through application of electrical potential. Thin layers of Ionomer are attached to flexible metallic electrodes and stacked together. Application of voltage causes interlayer adhesion at the interface between layers. The physical phenomenon responsible is known as the Johnsen-Rahbek effect (J-R). Research by Qin and McTeer (Qin and McTeer, 2007) and Sogard (Sogard et al., 2009) explorer this phenomenon compared to Coulomb forces in the context of electrostatic wafer chucks used in thin film processing. Both of these works highlight the importance of surface morphology at the interface to the overall forces generated in J-R chucks. Trapped particles or poor contact at the interface cause a significant loss of clamping force. A diagram of a J-R chuck is shown in Figure 2-10 and details effect of trapped particles.

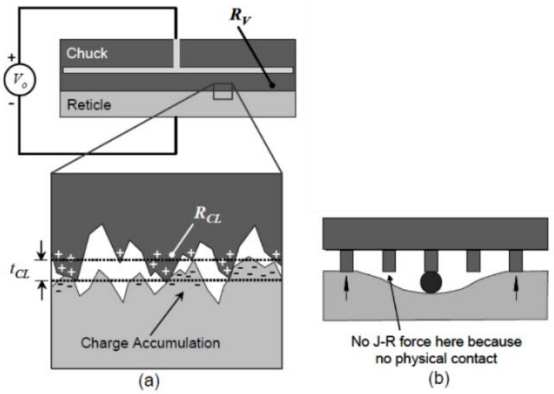

Figure 2-10: (a) Diagram of Johnsen-Rahbek chuck. R_V and R_{CL} are resistances in the bulk dielectric and contact layer respectivley, t_{CL} is contact layer thickness; (b) resulting pressure distribution from a trapped particle. (Sogard et al., 2009)

3.0 BACKGROUND AND MORPHING STRUCTURE DESIGN

The morphing structure explored in this work is composed of an actuator in the form of a diaphragm-type DEAP, and a variable stiffness structure in the form of a cantilevered beam. An interface post couples the actuator and beam together while a frame provides the support for the actuator and holds the two in the correct orientation. The general arrangement of the morphing structure is shown in Figure 3-1.

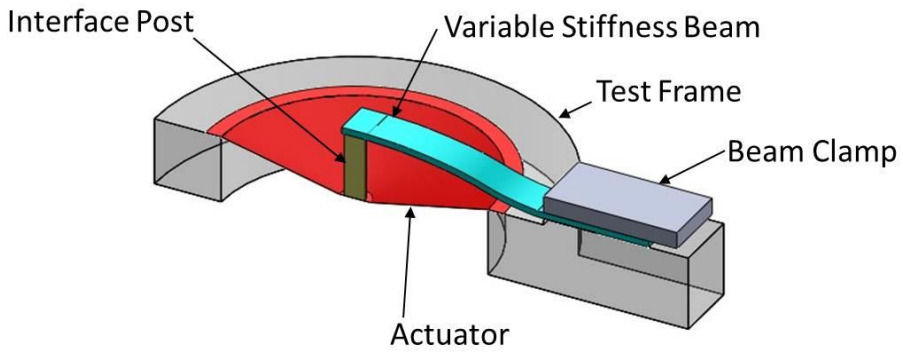

Figure 3-1: Morphing structure used in this work, highlighting the main components

In the equilibrium position, the beam is held in a deformed or bent state while the actuator has some initial deformation in the center of the diaphragm. When potential is applied to the actuator, the resulting compression in the thickness direction of the diaphragm in turn causes areal stretch in the radial direction. This is due to the incompressibility condition of the DEAP material. The radial stretch allows the diaphragm to deform more and thus the beam to deform

less or partially straighten. In this actuated state, the variable stiffness portion of the beam is then activated and the actuator turned off. The actuator diaphragm will attempt to contract in the radial direction and stretch in the thickness direction to return to equilibrium. As the beam has changed its effective modulus, the actuator cannot exert enough force to return the beam completely to the original position, thus a certain "hold" distance is present. This corresponds with a change in the structures shape via shape morphing.

3.1 DIELECTRIC ELECTROACTIVE POLYMER ACTUATOR

DEAP actuators can be made in many different form factors but are all based on the same principle design. A schematic showing the layout of the actuator type used is shown in Figure 3-2.

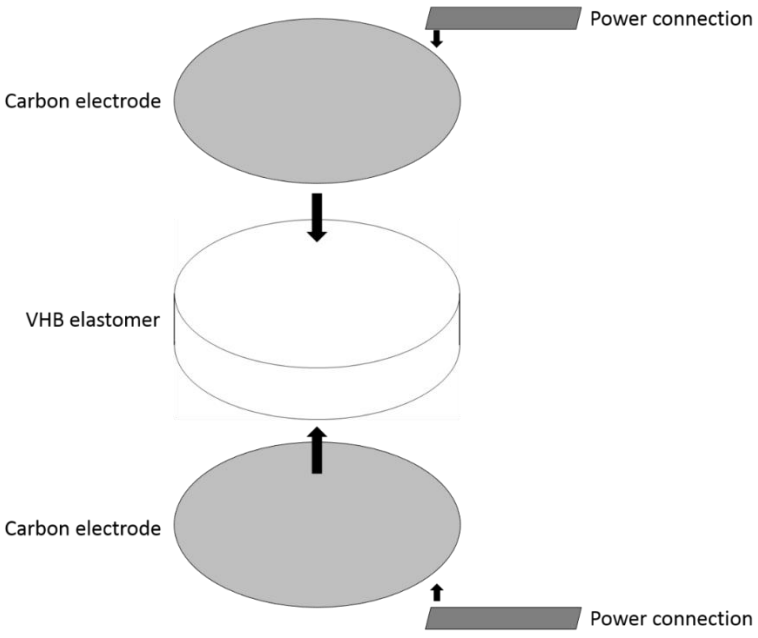

Figure 3-2: General construction of a dielectric electroactive polymer actuator used in this work

3M VHB tapes are an acrylic foam based family of double sided tape with pressure sensitive adhesive. Model 4905 is a clear, general purpose version in the 4910 family with a solid foam type and of an ideal thickness to fabricate actuators in the size range of interest. Mechanical properties of the 4910 family are shown in Table 3-1 and electrical properties are shown in Table 3-2.

Table 3-1: 3M 4905 Mechanical properties, (3M Company, 2014)

3M™ VHB™ Tapes				Adhesive and Foam			Release Liner		
Family	Number	Color	Tape Thickness Inches (mm) Tolerance	Adhesive Type	Foam Type	Density lb/ft³ (kg/m³)	Type	Thickness Inches (mm)	Color
4910	4905	Clear	0.020 (0.5) ± 15%	Gen Purp	Sollid	60 (960)	PE Film	0.005 (0.13)	Red (printed)
	4910	Clear	0.040 (1.0) ± 10%	Gen Purp	Sollid	60 (960)	PE Film	0.005 (0.13)	Red (printed)

3M™ VHB™ Tapes				Dynamic Adhesion Performance		
Family	Product Number	Color	Thickness Inches	90° Peel Adhesion lb/in N/cm	Normal Tensile lb/in² kPa	Dynamic Overlap Shear lb/in² kPa
4910	4905	Clear	0.020	12 (21)	100 (690)	70 (480)
	4910	Clear	0.040	15 (26)	100 (690)	70 (480)

3M™ VHB™ Tapes				Static Shear					Temperature Tolerance	
Family	Product Number	Color	Thickness Inches	72°F (22°C)	150°F (66°C)	200°F (93°C)	250°F (121°C)	350°F (177°C)	Short Term (Minutes, Hours) °F (°C)	Long Term (Days, Weeks) °F (°C)
4910	4905	Clear	0.020	1000	500	500			300 (149)	200 (93)
	4910	Clear	0.040	1000	500	500			300 (149)	200 (93)

Table 3-2: Electrical properties of 4905, (3M Company, 2014)

	3M™ VHB™ Tape 4950	4910	4611	Units	Test Standard
Dielectric Constant	2.28 1.99	3.21 2.68	2.80 2.43	at 1 kHz at 1MHz	ASTM D150 ASTM D150
Dissipation Factor	0.0227 0.0370	0.0214 0.0595	0.0130 0.0564	at 1 kHz at 1MHz	ASTM D150 ASTM D150
Dielectric Breakdown Strength	18 (460)	25 (630)	13 (330)	V/µm (V/mil)	ASTM D140
Thermal Conductivity (k value)	0.09 (0.6)	0.16 (1.1)	0.11 (0.8)	W/mK (BTU•in/hr•ft²•°F)	
Volume Resisitivity	1.5×10^{15}	3.1×10^{15}	1.4×10^{15}	Ω-cm	ASTM D257
Surface Resisitivity	$>10^{16}$	$>10^{16}$	$>10^{16}$	Ω/sq	ASTM D257
Water Vapor Transmission Rate	14.0			g/m²•day	ASTM F1249 at 38°C/1000% RH
Thermal Properties of Modeling					
Thermal Coefficient of Expansion	180 (100)			10^{-6} m/m/°C (10^{-6} in/in/°F)	
Shear Modulus (at 25°C, 1 Hz)	6×10^5			Pa	
Poisson's Ratio	0.49				

The 4910 group of VHB tapes is considered to be incompressible and viscoelastic in nature, and is widely used in DEAP fabrication. The viscoelastic properties increase the challenge of creating an accurate system model as relaxation of the material when subject to loading must be taken into account. The material has a fading memory (Wissler, 2014) and tends to relax under fixed strain and the stress approaches a stress value lower than the initial value when the strain was first applied. Relaxation tests and the viscoelastic model derived from them by Wissler will be used in this work as they are the most complete model for the 4910 group of materials available. A series of relaxation and tensile test results is plotted versus the simulation results by Wissler using the viscoelastic model in Figure 3-3. The number after the designator *Rel* (relaxation test) or *Ten* (tensile test) corresponds to the nominal strain in percent used in that particular test.

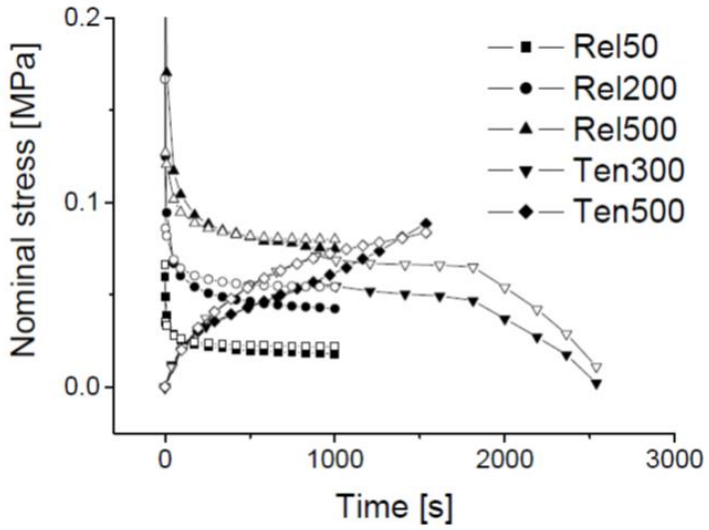

Figure 3-3: Relaxation experimental data (solid symbols) vs. simulation results (open symbols), (Wissler, 2014)

Plain powdered carbon electrodes are used in this work as they allow large strains in the actuator without constraining the elastomer and are relatively easy to work with. The powdered carbon used is from MTI Corporation and is sold as a conductive graphite powder for lithium-ion battery research with a granule size of 1-5 microns. These electrodes have a relatively high resistance, generally around one thousand ohms per centimeter. Despite this, no adverse effects were noted in the actuators fabricated for this work. Another common carbon-based electrode is a grease type, which is composed of carbon powder suspended in a high viscosity liquid. These electrodes can work well but are typically messy and tend to migrate from the initial area and potentially cause arcing at the electrical voltage levels present, so are avoided in this work.

3M CN-3190 tape is a thin, copper-nickel coated rip-stop polyester fabric tape with an electrically conductive pressure sensitive adhesive on one side. Typically used in EMI shielding applications, it also makes excellent flexible power connections for the actuator and the variable modulus layers. The adhesive's conductivity allows the connections to be made to both the aluminum and carbon powder electrodes without soldering or other mechanical means and the flexibility of the fabric allows for motion of the components during actuation without imposing forces from the high voltage wire and alligator clip connections. Properties for the tape are shown in Table 3-3.

Table 3-3: 3M CN-3910 tape properties, (3M Company, 2014)

Property (Test Method) (ASTM D1000 unless noted)	**Typical Value** US units (metric)
Color	Grey
Adhesive	Conductive acrylic
Type of Backing	Copper/Nickel coated ripstop polyester
Total Thickness (backing plus adhesive)	4.3 mils (0,11 mm)
Liner Thickness	5.8 mils (0,14 mm)
Breaking Strength	40 lb/in (18 kgf/25 mm)
Adhesion Strength	31 oz/in (900gf/25 mm)
Electrical Resistance Through Adhesive[1]	0.05 ohms

3.2 VARIABLE STIFFNESS STRUCTURE

The variable stiffness structure used in this work consists of an electroactive polymer, specifically an Ionomer, layer bonded to a metallic electrode, typically thin aluminum sheet. The Ionomer material was developed by the Dr. Tara Meyer research group of the University of Pittsburgh department of Chemistry. A collaborative effort between the Meyer group and the Dr. William Clark research group in the Department of Mechanical Engineering and Materials Science at the University of Pittsburgh has produced the variable stiffness structures used in this work. Another important contribution of this cooperative effort has been the development of methods to characterize the properties of these structures. The Ionomer used is based on poly(ethelyne-co-acrylic-acid) that has been reacted with aqueous tetramethylammonium hydroxide. A simplified diagram of the reaction is shown in Figure 3-4.

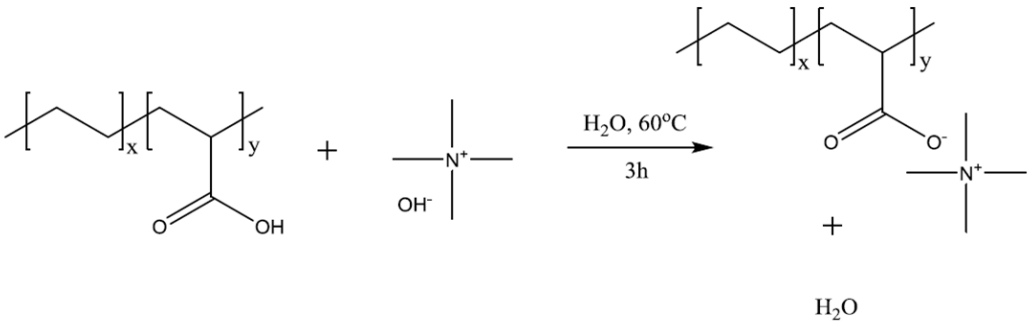

Figure 3-4: Structural diagram of reaction used to create Ionomer (Ladd, 2015)

The resulting material, poly(ethylene-co-tetramethylammoniumacrylate) has active components in the mobile positive tetramethylammonium ions, with the negative carboxylates generally stationary in the polymer framework. The mobility of the positive ions is responsible for the specific electroactive properties exhibited by the material, namely the Johnsen-Rahbek

effect when fabricated in the form used in this work. The variable stiffness structures used here are a type of composite beam, composed of two Ionomer/electrode layers placed between two thin metallic outer leaves. This arrangement preserves symmetry about the neutral axis. Prior work has been done by the Meyer and Clark groups to measure the change in effective modulus of the Ionomer/electrode layer portion of the beam when potential is applied. This testing was performed using a bending unit configured for three point and cantilever loading. Tests were performed for two layer (one interface) beams in three point and cantilever modes to show the effect of the boundary conditions of the structure on its ability for stiffness variation. The plot shown in Figure 3-5 shows the change in force plotted against displacement for a two layer Ionomer beam in three-point bending subject to 500 volts in active mode versus the same beam with no voltage applied. The effective modulus of the beam changes from 16 to 37 MPa with the application of the potential. This corresponds to a multiplication factor of 2.3 of the effective modulus when the voltage is applied for three point bending.

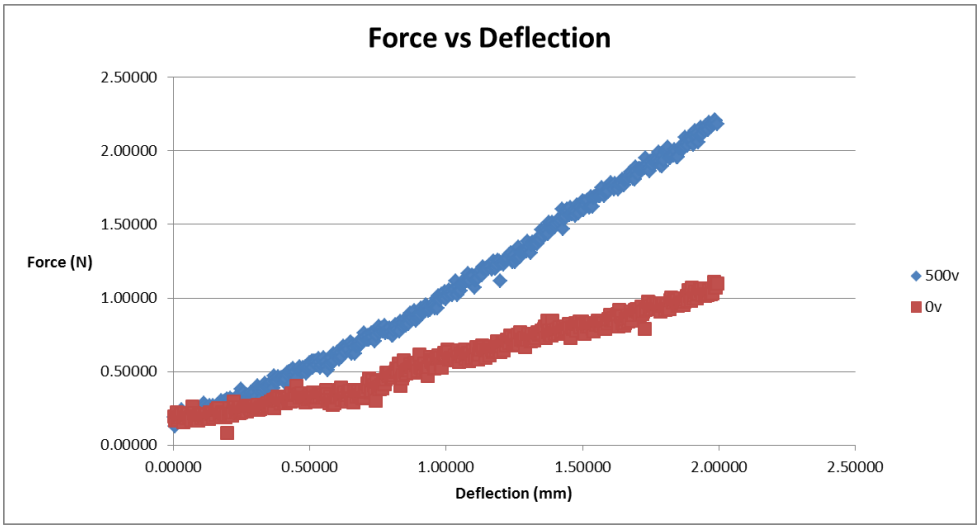

Figure 3-5: Force vs. deflection data for passive and active states of a variable stiffness Ionomer beam structure in three-point bending

The plot shown in Figure 3-6 shows the change in force plotted against displacement for a composite two layer Ionomer and two stainless outer layer beam in cantilever bending subject to 500 volts in active mode versus the same beam with no voltage applied. For the cantilever test shown, the beam incorporated the outer stainless cover layers to match the design used in this work. As such, it has a higher effective modulus than the Ionomer/electrode layer only beam tested in three point mode. This allows the determined effective modulus multiplication factor to be used in the analytical modeling but precludes the results from use in determining the exact effect of the boundary conditions. The effective modulus of the beam changes from 522 to 746 MPa with the application of the potential. This corresponds to a multiplication factor of 1.4 of the effective modulus when the voltage is applied in cantilever mode for the composite beam.

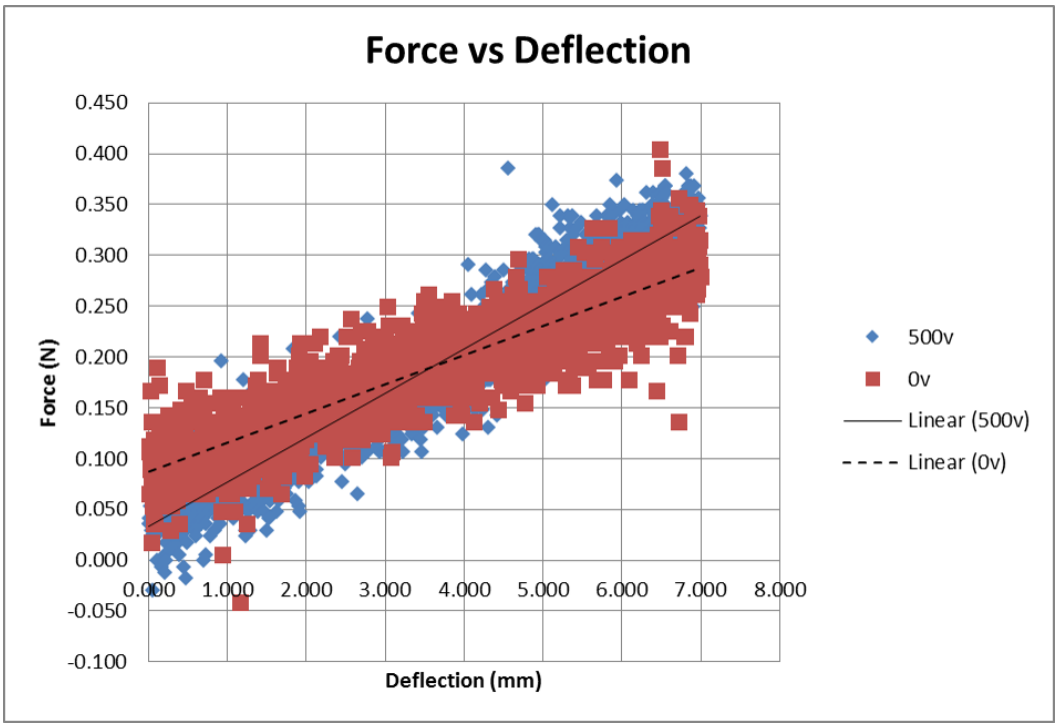

Figure 3-6: Force vs. deflection data for passive and active states of a variable stiffness Ionomer beam structure in cantilever bending. The linear trend lines show the change in slope when the Ionomer is activated

One can determine the relative performance of the variable stiffness structures used here through the use of second moment of area analysis. For a two layer beam, if a frictionless interface is assumed, the second moment of area for the composite would be that of a homogenous beam with the cross section of the two layers side by side rather than stacked. For a perfectly bonded interface, the second moment of area for the composite would be that of a homogenous beam with the cross section of the two layers stacked on top of each other. This is shown graphically in Figure 3-7.

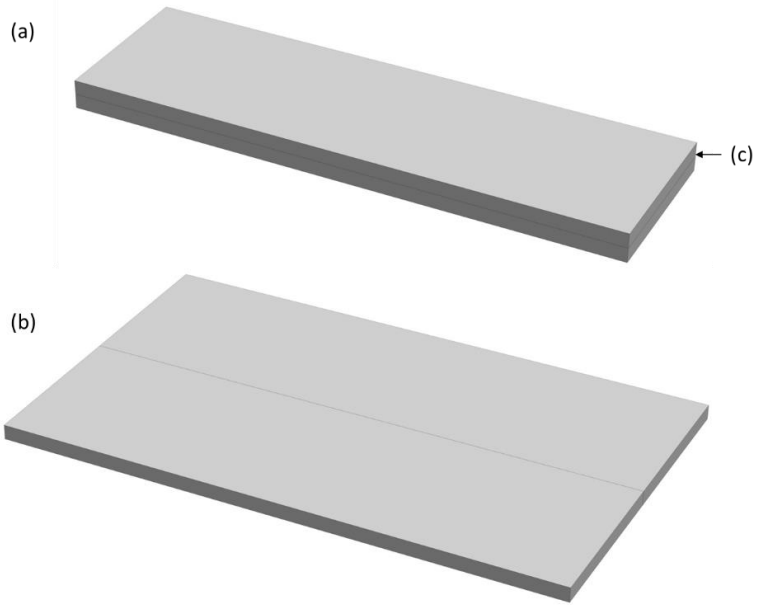

Figure 3-7: Example of bilayer area moment analysis; (a) bilayer beam with interface (c), (b) effective section of (a) if (c) is assumed frictionless

For a given two layer beam geometry, force and displacement, this change in second moment of area from a frictionless interface to a perfectly bonded interface corresponds to a multiplication factor of 4 for the effective modulus of the beam. Equation 3.1 for a perfectly bonded homogenous section and 3.2 for a frictionless interface effective section show this relation.

$$I = \frac{1}{12} bh^3 \tag{3.1}$$

$$I = \frac{1}{12} * 2b\left(\frac{h}{2}\right)^3 = \frac{bh^3}{48} \tag{3.2}$$

Thus, the structure used in this work is capable of 57% of a perfect stiffness variation in three point bending and 35% effective in cantilever bending as part of an Ionomer and stainless steel composite beam.

In order to demonstrate relationship of the change in effective modulus to the voltage applied, a series of tests were performed in 50 volt increments beginning at no applied voltage and ending at 450 volts. This series of test was repeated three times. The effective modulus for a two layer Ionomer structure was calculated at each voltage step and is plotted versus the applied voltage Figure 3-8 for each of the three test series. This shows the relationship between applied potential and the resulting change in effective modulus. Though the relationship is non-linear, control of the stiffness to any intermediate value between the flexible and rigid states should be possible with a fine enough resolution of voltage control.

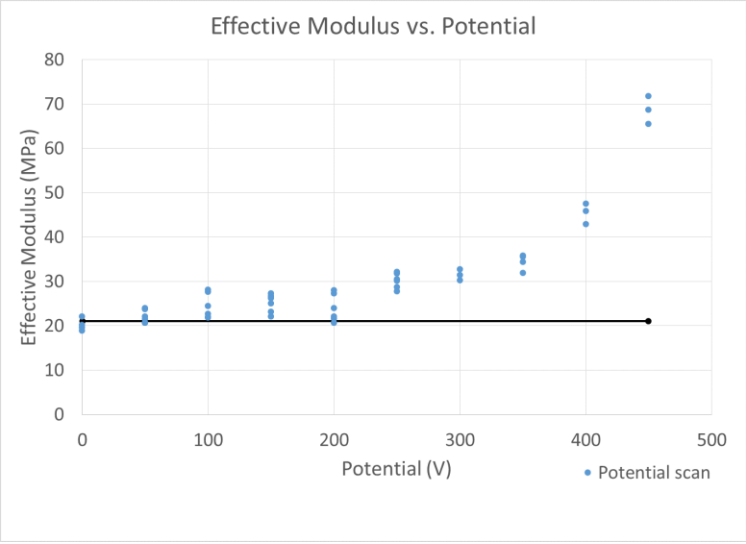

Figure 3-8: Plot of effective modulus vs. applied potential for two layer Ionomer structure

4.0 MODELING

In order to quantify the performance of the morphing structure and provide a means of comparing alternate structural designs, an analytical model was developed. The analytical model for the morphing structure in this work is composed of two independent models, one for the actuator and one for the variable stiffness structure. The coupling method chosen to relate these models relies on the principle of energy conservation and equivalence through the balance of forces. Focus is placed on a static model to highlight the most important feature of the structure, shape change through effective modulus variation. The dynamics of the structural response are essentially ignored in this work but could be equally as important to predict for certain applications.

The combined model developed here is implemented in a MATLAB© script for the numerical simulations.

4.1 DEAP HYPERELASTIC MODEL

A hyperelastic model was formulated using the Ogden form of the strain energy density function, (R. W. Ogden, 1972). Using research on the 4910 family of VHB tapes published by Wissler (Wissler, 2014), values for the hyperelastic coefficients may be used directly, as they have been

validated experimentally in that work. Table 4-1 shows the experimentally optimized hyperelastic coefficients for the Ogden formulation.

Table 4-1: Optimized hyperelastic coefficients for the Ogden strain energy density formulation, (Wissler, 2014)

μ_1 [MPa]	α_1 [-]	μ_2 [MPa]	α_2 [-]	μ_3 [MPa]	α_3 [-]
0.0858	1.293	0.0843	2.3252	-0.0233	2.561

Where the following relation of the conventional isotropic shear modulus μ is related to the hyperelastic coefficients by the relation:

$$2\mu = \sum_{i=1}^{N} \mu_i \alpha_i \tag{4.1}$$

Where N is the number of hyperelastic parameters used to fit the experimental data for the material used. In the case of VHB, the three parameter model by Wissler shown in Table 4-1 is sufficient to fit the experimental data.

The DEAP model constructed for this work calculates principal stresses in the elastomer for the fabrication state, the equilibrium state and in the actuated state. From the stress component in the radial direction, the force in the radial direction and thus the force projection on the axial direction may be found as a function of the center displacement. In the actuation state, the Maxwell stress contribution from the electric field is added to the elastic stress. The resulting combined stress is used to determine the new axial force for the actuator.

4.1.1 Actuator fabrication state

Labeled state "1" in the corresponding calculations, this state determines the total strain energy contained in the actuator during the fabrication process and subsequent relaxation period due to material viscoelasticity. The fabrication state corresponds to a biaxial stretching of an incompressible material volume. This fabrication deformation and the geometry variables used to describe it are shown in Figure 4-1. Due to the axisymmetric nature of the actuator used in this work, a cylindrical coordinate system was chosen for the model.

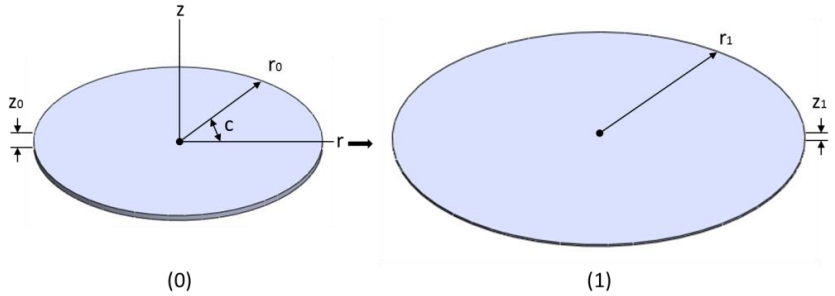

Figure 4-1: Fabrication state deformation geometry variables for: (0) initial and (1) fabrication states

The geometry of said volume is labeled as state "0" in the initial un-stretched state. We define the initial (0) geometry as follows:

$$unstretched\ radius: r_0$$

$$unstretched\ thickness: z_0$$

We define the stretched or fabricated (1) state geometry as follows:

$$stretched\ radius: r_1$$

$$stretched\ thickness: z_1$$

And define the following variables:

$$radial\ (r)\ principal\ stretch: \lambda_r$$

$$circumfrential\ (c)\ principal\ stretch: \lambda_c$$

$$thickness\ (z)\ principal\ stretch: \lambda_z$$

$$strain\ energy\ density: \psi$$

$$radial\ stress: \sigma_r$$

$$circumfrential\ (c)\ stress: \sigma_c$$

$$thickness\ stress: \sigma_z$$

From the material incompressibility constraint, we can determine the following relations for the principle stretches:

$$\lambda_r \lambda_c \lambda_z = 1 \tag{4.2}$$

$$\lambda_r = \frac{r_1}{r_0} \tag{4.3}$$

$$\lambda_c = \lambda_r \tag{4.4}$$

$$\lambda_z = \frac{z_1}{z_0} \tag{4.5}$$

Following this, the radial stress in the Ogden formulation may be found using the following:

$$\psi = \sum_{i=1}^{N} \frac{\mu_i}{\alpha_i} \left(\lambda_r^{\alpha_i} + \lambda_c^{\alpha_i} + \lambda_z^{\alpha_i} - 3\right) \tag{4.6}$$

$$\sigma_r = \sigma_c = \lambda_r \frac{\partial \psi}{\partial \lambda_r} - \lambda_z \frac{\partial \psi}{\partial \lambda_z} \tag{4.7}$$

$$\lambda_r \frac{\partial \psi}{\partial \lambda_r} = \sum_{i=1}^{N} \mu_i \lambda_r^{\alpha_i} \ \ and \ \ \lambda_z \frac{\partial \psi}{\partial \lambda_z} = \sum_{i=1}^{N} \mu_i \lambda_z^{\alpha_i} \tag{4.8}$$

Thus:

$$\sigma_r = \sum_{i=1}^{N} \mu_i \left(\lambda_r^{\alpha_i} - \lambda_z^{\alpha_i}\right) \tag{4.9}$$

As this state has no axial loading applied by the variable modulus structure to mechanically bias it, the solution for the axial force is zero as the radial direction is orthogonal to the axial direction.

4.1.2 Actuator equilibrium state (2)

Labeled state "2" in the corresponding equations, this state corresponds to the deformation of the actuator in the static equilibrium position with the variable stiffness structure. As the deformation of the actuator is more complex in the equilibrium and subsequent states than in the fabrication state, we define a new set of geometry variables following the same convention to describe it. A graphical representation of this deformation and the geometry variables used to describe it is shown in Figure 4-2.

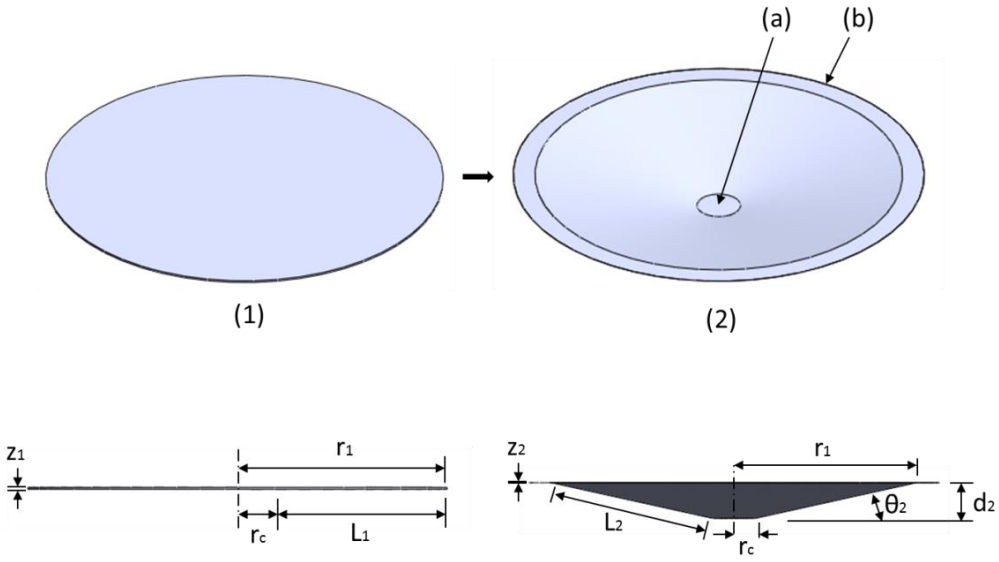

Figure 4-2: Equilibrium state deformation geometry variables for: (1) fabricated and (2) equilibrium states; (a) indicates a circular area of radius r_c at the diaphragm center where the interface post is attached. This area is assumed to be rigid. (b) Indicates the fixed area where the diaphragm is attached to the frame. This is shown for reference and is not included in the model. The fabrication radius r_1 is shown on the state figure to highlight this.

We define two additional geometry variables for the fabrication state (1) as follows:

$center\ fixed\ radius: r_c$

$active\ annular\ length: L_1$

With the following geometric relation:

$$r_1 = r_c + L_1 \tag{4.10}$$

We define the equilibrium (2) state geometry variables as follows:

$thickness: z_2$

$axial\ displacement: d_2$

$active\ annular\ length: L_2$

We define the following geometrical relations of force and stress shown in Figure 4-3 for the subsequent states and define the area A as the surface area of the cylindrical portion of the actuator elastomer assumed fixed by the rigid interface disk for each state defined by the z value used. In other words, A is the cylindrical cross-sectional area of the actuator material where the deformed region of the actuator attaches to the rigid region under the interface post. This surface area is used to determine the radial force in the diaphragm from the radial stress.

$$A = 2\pi r_c z \tag{4.11}$$

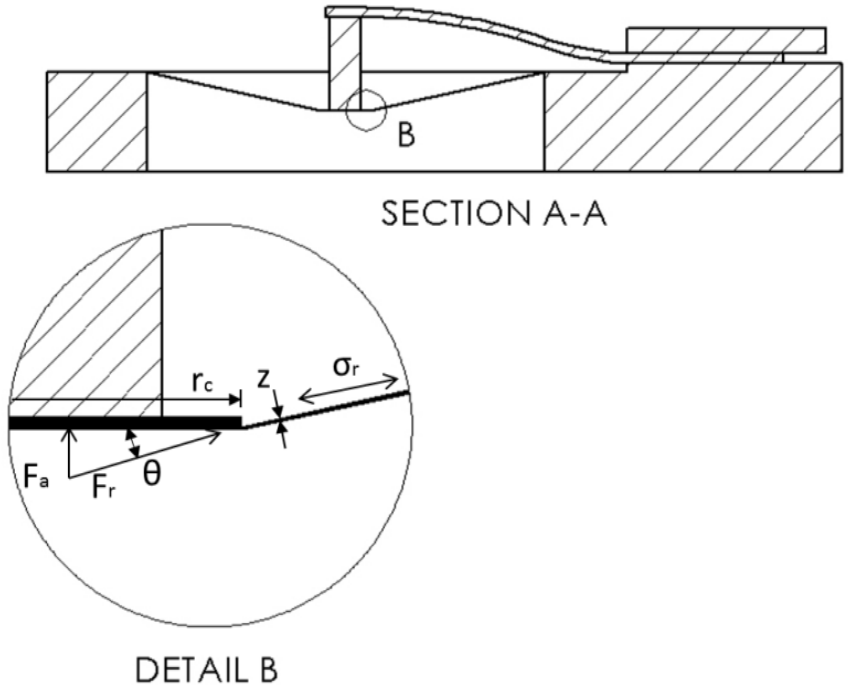

Figure 4-3: Section view and detail of the morphing structure to illustrate force and stress geometrical relations; F_r is radial force in the actuator, F_a is the axial projection of F_r, σ_r is the radial stress in the actuator, θ is the angle formed between the actuator and the horizontal plane, r_c is the radius of the center interface disk, z is the diaphragm thickness

Following a similar approach as the approach used in the fabrication state derivation, and using the incompressibility relation (4.1), the principal stretches can be defined as:

$$\lambda_r = \frac{L_2}{L_1} \tag{4.12}$$

$$\lambda_c = 1 \tag{4.13}$$

$$\lambda_z = \frac{z_1}{z_0} = \frac{L_1}{L_2} \tag{4.14}$$

Using the Pythagorean Theorem, the following relation is obtained for the annular length L_2:

$$L_2 = \sqrt{{L_1}^2 + {d_2}^2} \tag{4.15}$$

And the relation for theta used in the force projection is:

$$\sin\theta_2 = \frac{d_2}{L_1}\left[1 + \left(\frac{d_2}{L_1}\right)^2\right]^{-1/2} \tag{4.16}$$

Thus the radial force and its axial projection in the actuator can be determined for the current stretches as:

$$\sigma_r = \sum_{i=1}^{N} \mu_i\left(\lambda_r^{\alpha_i} - \lambda_z^{\alpha_i}\right) \tag{4.17}$$

$$A_2 = 2\pi r_c z_2 \tag{4.18}$$

$$Fr_2 = \sigma_r * A_2 \tag{4.19}$$

$$Fa_2 = Fr_2\, sin(\theta_2) \tag{4.20}$$

4.1.3 Actuator on "actuated" state (3)

Labeled state "3" in the corresponding equations, this state corresponds to the deformation of the actuator when voltage is applied. Due to the electromechanical coupling, there are several approaches to modeling the actuation state. The one used here is based on the formulation by Wissler, (Wissler, 2014) in which the Maxwell stress in the thickness direction due to electrostatic forces is determined and the resulting combined elastic and electrostatic form of the radial stress is found. The geometric variables for the actuated state are shown in Figure 4-4.

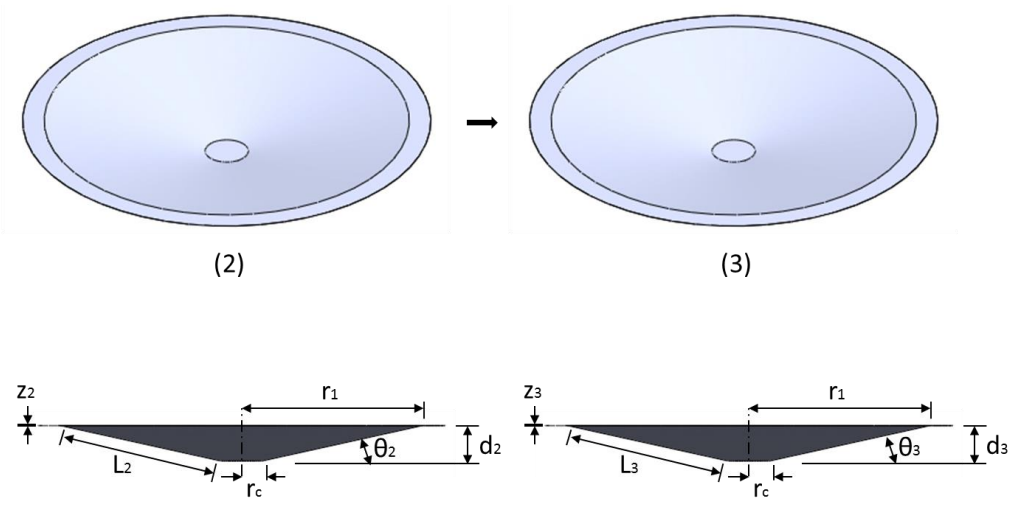

Figure 4-4: Actuated state deformation geometry variables for: (2) equilibrium and (3) actuated states

Again, the principal stretches for state 3 can be defined as:

$$\lambda_r = \frac{L_3}{L_2} \tag{4.21}$$

$$\lambda_c = 1 \tag{4.22}$$

$$\lambda_z = \frac{L_2}{L_3} \tag{4.23}$$

Using the Pythagorean Theorem, the following relation is obtained for the annular length L_3:

$$L_3 = \sqrt{{L_1}^2 + {d_3}^2} \tag{4.24}$$

And the relation for theta used in the force projection is:

$$\sin\theta = \frac{d_3}{L_1}\left[1 + \left(\frac{d_3}{L_1}\right)^2\right]^{-1/2} \tag{4.25}$$

We define three additional parameters for the electrostatics portion of the actuated state (3) model as follows:

$applied\ actuator\ voltage$: Φ

$relative\ permitivity\ of\ the\ elastomer$: ϵ_r

$permitivity\ of\ vacuum$: ϵ_0

The pressure or Maxwell stress due to the electrostatic forces in the thickness direction is given by:

$$P_{el} = \epsilon_r \epsilon_0 \left(\frac{\Phi}{z_3}\right)^2 \tag{4.26}$$

And the resulting form of the radial stress is the elastic term minus the electrostatic term:

$$\sigma_r = \sum_{i=1}^{N} \mu_i \left(\lambda_r^{\alpha_i} - \lambda_z^{\alpha_i}\right) - P_{el} \tag{4.27}$$

The forces can thus be found in the same manner as the previous state:

$$A_3 = 2\pi r_c z_3 \tag{4.28}$$

$$Fr_3 = \sigma_r * A_3 \tag{4.29}$$

$$Fa_3 = Fr_3\, sin(\theta_3) \tag{4.30}$$

4.1.4 Actuator off state (4)

Labeled state “4” in the corresponding equations, this state corresponds to the deformation of the actuator when the voltage is removed, and subsequently the new equilibrium position. As it is the reverse of the actuation step, a contraction in the radial direction and an expansion in the thickness direction are experienced. For an ideal actuator with negligible viscoelastic effects, state “4” and “2” will be identical if the mechanical bias load is constant between them. The geometric variables for the actuated state are shown in Figure 4-5.

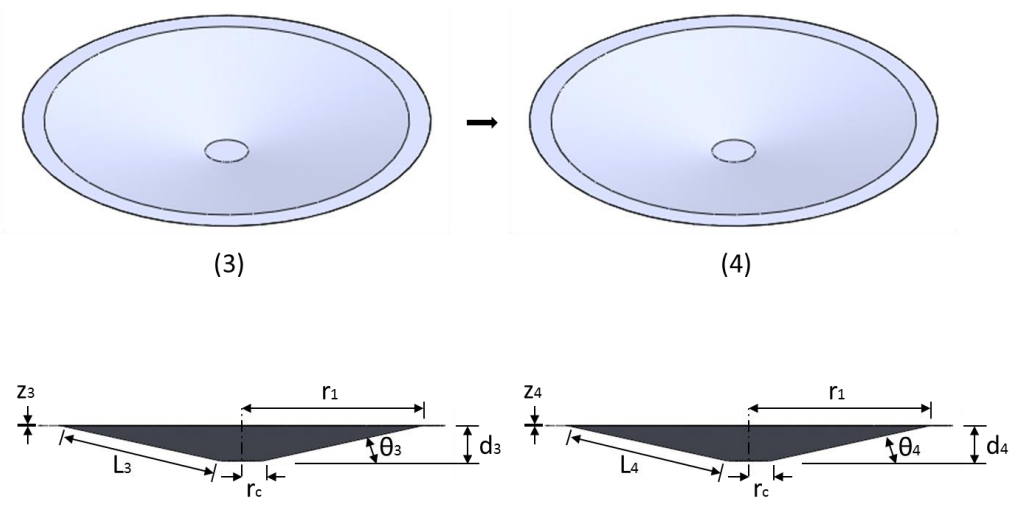

Figure 4-5: Actuator off state deformation geometry variables for: (3) actuated and (4) new equilibrium states

Again the principal stretches for state 4 can be defined as:

$$\lambda_r = \frac{L_4}{L_3} \tag{4.31}$$

$$\lambda_c = 1 \tag{4.32}$$

$$\lambda_z = \frac{L_3}{L_4} \tag{4.33}$$

Using the Pythagorean Theorem, the following relation is obtained for the annular length L_4:

$$L_4 = \sqrt{{L_1}^2 + {d_4}^2} \tag{4.34}$$

And the relation for theta used in the force projection is:

$$\sin\theta = \frac{d_4}{L_1}\left[1 + \left(\frac{d_4}{L_1}\right)^2\right]^{-1/2} \tag{4.35}$$

Thus the radial force and its axial projection in the actuator can be determined for the current stretches as:

$$\sigma_r = \sum_{i=1}^{N} \mu_i\left(\lambda_r^{\alpha_i} - \lambda_z^{\alpha_i}\right) \tag{4.36}$$

$$A_4 = 2\pi r_c z_4 \tag{4.37}$$

$$Fr_4 = \sigma_r * A_4 \tag{4.38}$$

$$Fa_4 = Fr_4\, sin(\theta_4) \tag{4.39}$$

4.2 VARIABLE STIFFNESS STRUCTURE MODEL

The variable stiffness structure used in this work is in the general form of a cantilever beam. The un-bonded composite nature of its construction prevents the use of unmodified simple beam models due to frictional effects in the interfaces between layers. The modelling method chosen uses a slightly modified beam model with experimentally validated properties. A simple solution form using the Euler-Bernoulli beam theory is used with the elastic modulus term chosen as an effective modulus for a homogenous beam matching the geometric properties of the composite beam. The values for this effective modulus are determined experimentally using bending tests.

4.2.1 Beam deflection model

The beam model used here uses the familiar Euler-Bernoulli solution to the beam bending problem with cantilever and concentrated end load boundary conditions. While typically reserved for approximating small deflections in linear elastic models, it is used here for simplicity. The more accurate solutions available that incorporate shear effects, the Timoshenko model for example, would likely yield a closer approximation. The issue with applying this model here is the lack of experimentally determined material property data for the Ionomer used. The model is formulated with the beam geometry as shown in Figure 4-6.

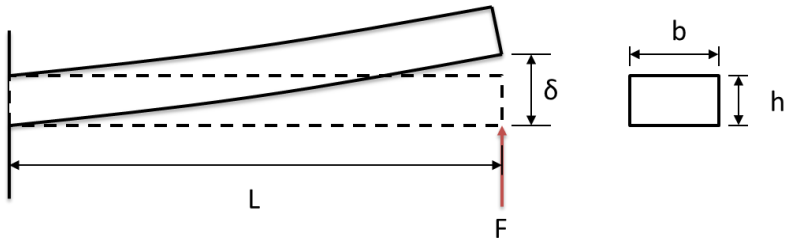

Figure 4-6: Cantilever beam loading geometry

We define the beam geometry variables as follows:

$beam\ length: l$

$end\ deflection: \delta$

$beam\ width: b$

$beam\ thickness: h$

$passive\ effective\ elastic\ modulus: E$

The second moment of area about a center neutral axis may be found:

$$I = \frac{1}{12} bh^3 \tag{4.40}$$

The solution to determine the applied force in terms of the other variables for each state (i), takes the following form:

$$F_i = \frac{3EI\delta_i}{l^3} \tag{4.41}$$

4.2.2 Modulus variation

The effective modulus multiplication factor k that was experimentally determined in chapter 3 can be applied in the model for the active state of the variable stiffness beam. This factor is applied as:

$$E_{on} = k * E \tag{4.42}$$

For:

$active\ effective\ elastic\ modulus: E_{on}$

$multiplication\ factor: k$

4.3 COMBINED SYSTEM MODEL

The actuator and beam models are coupled through force equivalence. The following relation is used to complete the system as a function of the displacement d_i of the actuator. The total interface length is simply the length of the interface post minus any offset distance between the

bottom of the beam and the actuator surface. The completed system may then be solved for d_i in each force balance equilibrium state.

$$\delta_i = total\ interface\ length - d_i \tag{4.43}$$

4.3.1 Equilibrium state (2)

The equilibrium state position is found by solving the following equality for the independent variable d_2:

$$Fa_2 = Fb_2\ or\ Fr_2\ sin(\theta_2) = \frac{3EI\delta_2}{l^3} \tag{4.44}$$

4.3.2 Actuator on, "actuated" state (3)

The actuated state position is found in a similar manner as in the equilibrium case. Solving the following equality for the independent variable d_3:

$$Fa_3 = Fb_3\ or\ Fr_3\ sin(\theta_3) = \frac{3EI\delta_3}{l^3} \tag{4.45}$$

4.3.3 Modulus activation

While not a discrete state in the model formulation, the increase in the beams effective elastic modulus corresponds to the variable stiffness structure being activated while the actuator is still on, and due to complexity, should be discussed in a separate section.

The formulation used here of a multiplying factor k for the active effective elastic modulus is relatively simple. However, the active effective modulus cannot be substituted into the equations as in the previous states. Since the beam was deflected in the weaker, passive state, if one simply substituted the active effective elastic modulus, the model would predict an increase in d_4 with no other perturbation of the system. This isn't realistic given the form of the variable stiffness structure used here. Activation will stiffen it in its current shape rather than cause it to change shape abruptly. This behavior would be more characteristic of a shape memory material.

This can also be visualized if the coupling in the structure is put in terms of energy rather than purely in terms of force. A certain amount of energy is required to deflect a beam a constant distance δ for a given beam geometry and modulus. If the modulus is increased, the energy required increases proportionally. Since the variable stiffness beam in our case has been deflected in the weak state, the energy in the system corresponds to this effective modulus. Once the effective modulus is increased via electric potential, the mechanical energy in the beam hasn't increased.

4.3.4 Actuator off "hold" state (4)

The position for state 4 is cannot be determined directly as in the previous states. This is due to the change in the beam stiffness and thus a separate formulation is used. First the change in force from state 3 to 4 in the actuator:

$$\Delta F_4 = Fa_3 - Fa_4 \tag{4.46}$$

Then, the change in the tip deflection for the beam can be formed as:

$$\Delta\delta_4 = \frac{\Delta F_4 l^3}{3E_{on}I} \tag{4.47}$$

The new position can subsequently be found from:

$$\delta_4 = \delta_3 + \Delta\delta_4 \tag{4.48}$$

And finally:

$$d_4 = total\ interface\ length - \ \delta_4 \tag{4.49}$$

This system can then be solved to determine d_4.

5.0 FABRICATION

5.1 DIELECTRIC ELECTROACTIVE POLYMER ACTUATOR

The DEAP actuator is fabricated in a similar manner as others described in literature of the diaphragm type using the 3M 4910 group of VHB tapes as the elastomer. A 25 mm square piece of 4905 is stretched over an acrylic frame with a 50 mm internal diameter, so as to completely cover the opening in the ring. This acrylic ring acts as both the supporting frame for the actuator and the base of the test fixture. In order to handle the elastomer for stretching and not damage the adhesive on both sides, the red polyethylene backing material from the VHB tape is recycled and used as a grip. After removal from the VHB, the backing is cut into strips and re-adhered to the corners of the VHB square. As the adhesive on the VHB is pressure sensitive (PSA), a small amount of pressure is used to allow the poly to release easily after the VHB has been adhered to the frame. The VHB is first stretched at the corners across the frame. The backing material pieces are then moved from the corners to the sides and each side is subsequently stretched out and adhered to the frame. A pictorial sequence of the VHB stretching process is shown in Figure 5-1.

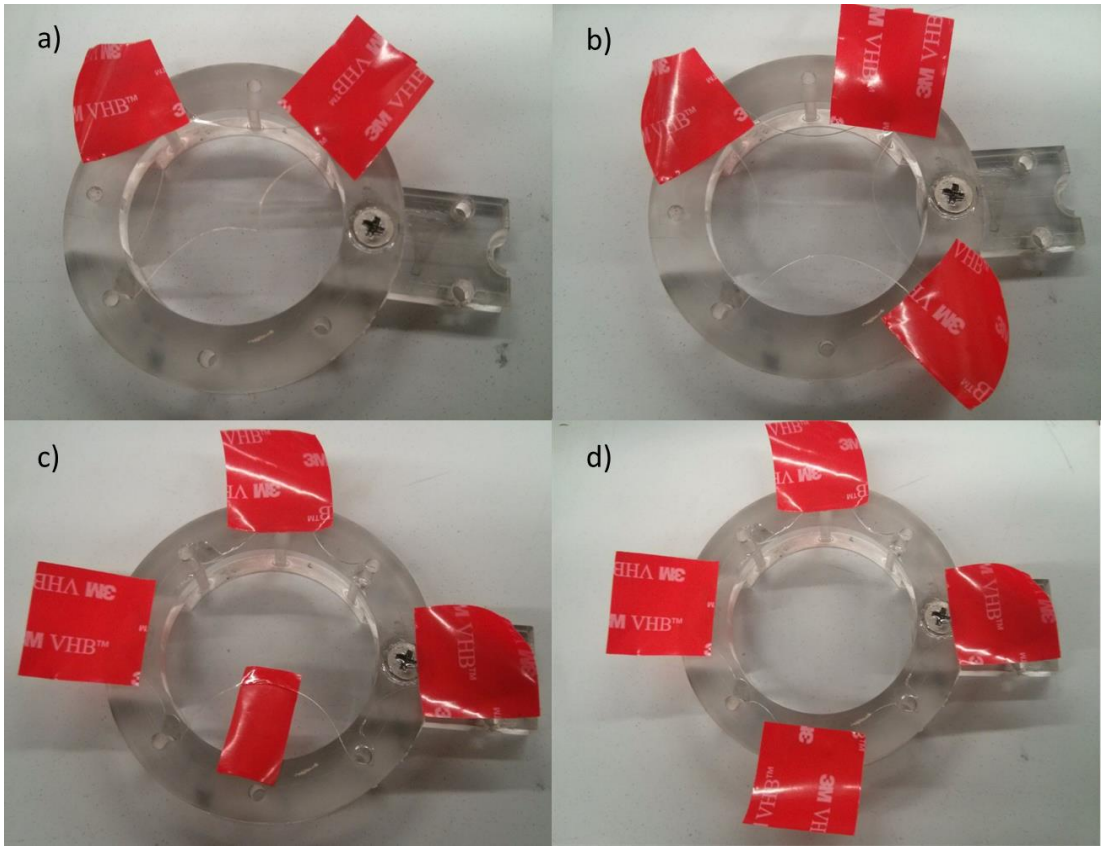

Figure 5-1: VHB elastomer stretching sequence showing the use of the red poly backing material to prevent damage to the VHB while stretching over the frame; a) first three corners are stretched and adhered to the frame, b) final corner stretched out and adhered, c) final side being stretched out, d) completed VHB diaphragm prior to the removal of the backing material grips

The PSA on the VHB is pressed on and allowed to adhere directly to the clean acrylic surface, affixing it to the ring in its stretched state. This initial stretch will be referred to as "pre-stretch" and this configuration of the elastomer as the "fabrication" state in this work. The pre-stretch is shown in Figure 5-2 to illustrate the first and second principal stretch value determination. It is somewhat obvious from Figure 5-2 that the first two principal stretches are not constant over the entire area of the elastomer and thus neither is the third. This precludes the determination of the third stretch by the first two and the incompressibility condition. Thus, the

third principal stretch must be determined by direct thickness measurement of the fabricated diaphragm. While the stretches may not be uniform over the entire volume, they are relatively uniform over the volume of the active diaphragm and thus allow a relatively simple model to be used.

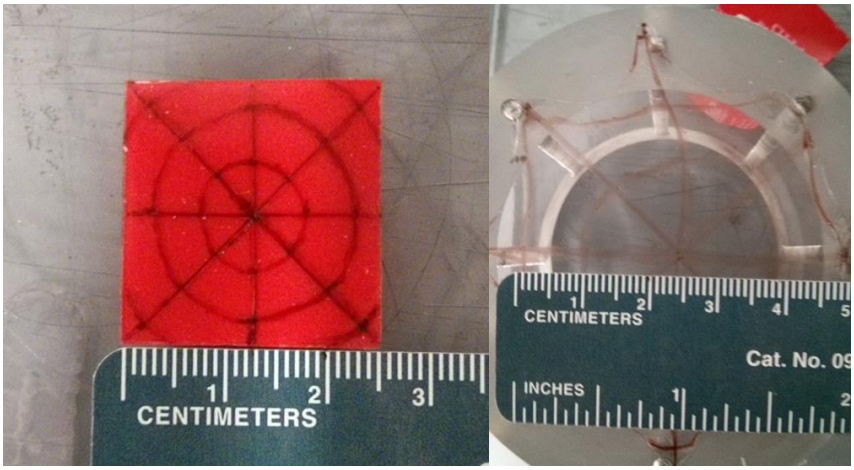

Figure 5-2: Photo of un-stretched 4905 VHB elastomer (left) and stretched VHB to form diaphragm, the markings are to illustrate principle stretch measurements only

A polyethylene coated paper stencil is placed over the VHB diaphragm to mask the border during the electrode deposition and a 6mm diameter, 0.08mm thick plastic disk is placed in the center of the top face of the diaphragm. This disk acts as a support for the interface post to the variable stiffness beam. The top face circular electrode is subsequently deposited by brushing carbon particulate powder on both sides of the VHB using a cotton swab. The paper masks are used to control the size and shape of the resulting electrode. This prevents the buildup of powder in the corner formed by the VHB and acrylic on one side and produces a corresponding electrode of similar diameter on the open face. The masking and deposition process is shown in Figure 5-3, note that after the top face electrode is completed; the mask is replaced with a blank piece of coated paper to protect the electrode face while working on the bottom electrode.

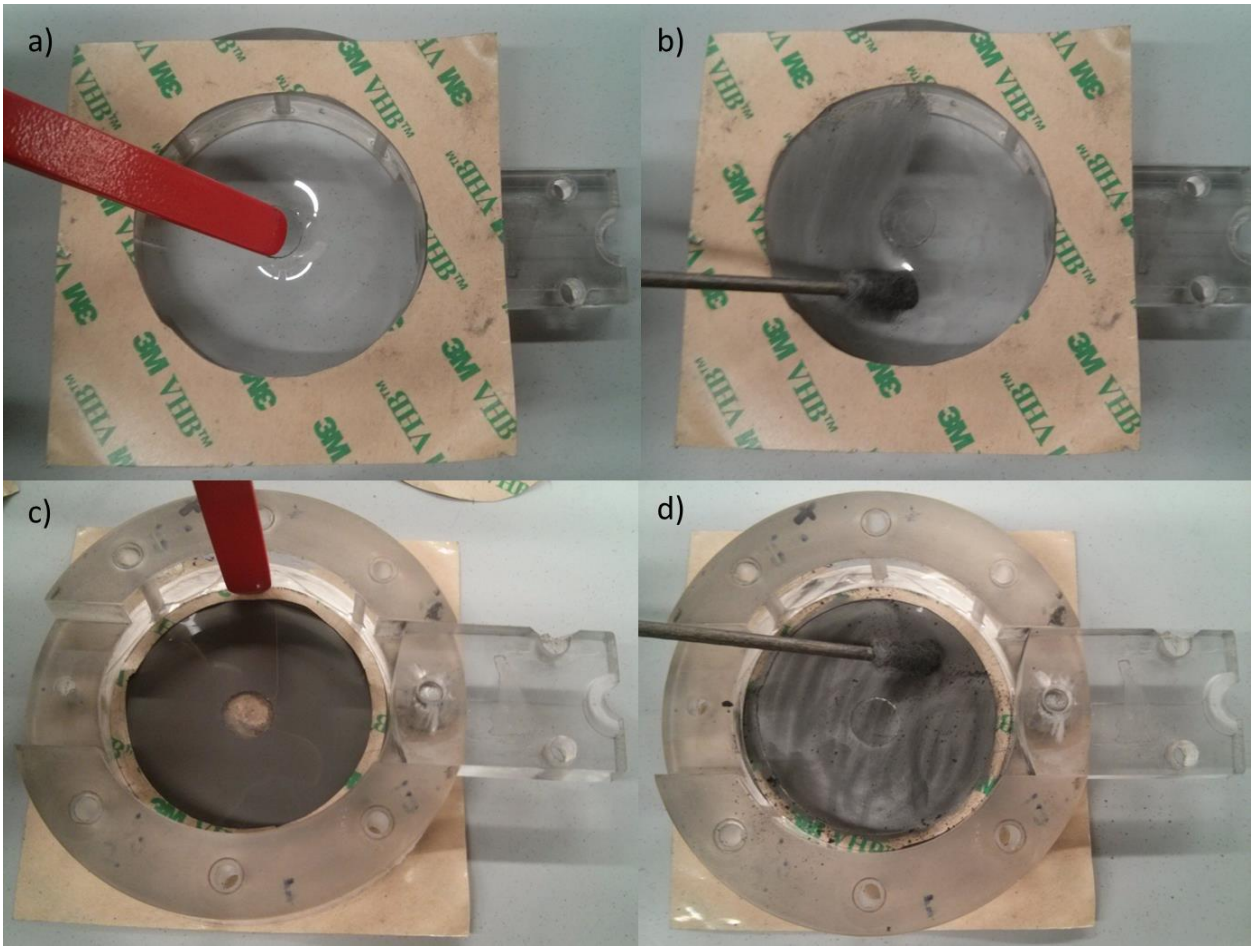

Figure 5-3: Electrode masking and deposition; a) top face mask and center disk being pressed into place, b) upper electrode being brushed on with a cotton swab, c) the bottom face mask being applied, d) bottom face electrode being brushed on

Connections are formed from strips of 3M CN-3910 tape and adhered to each electrode. The resistance from the connections to the opposite edge of each electrode is measured to ensure it is not higher than three thousand ohms over the area. The resistance is then measured between the connections to ensure there are no short circuits between the electrodes. The electrical connections, a completed actuator and the resistance testing process are shown in Figure 5-4. The plastic disk is visible at the center of the top of the diaphragm as the small area where no electrode is deposited.

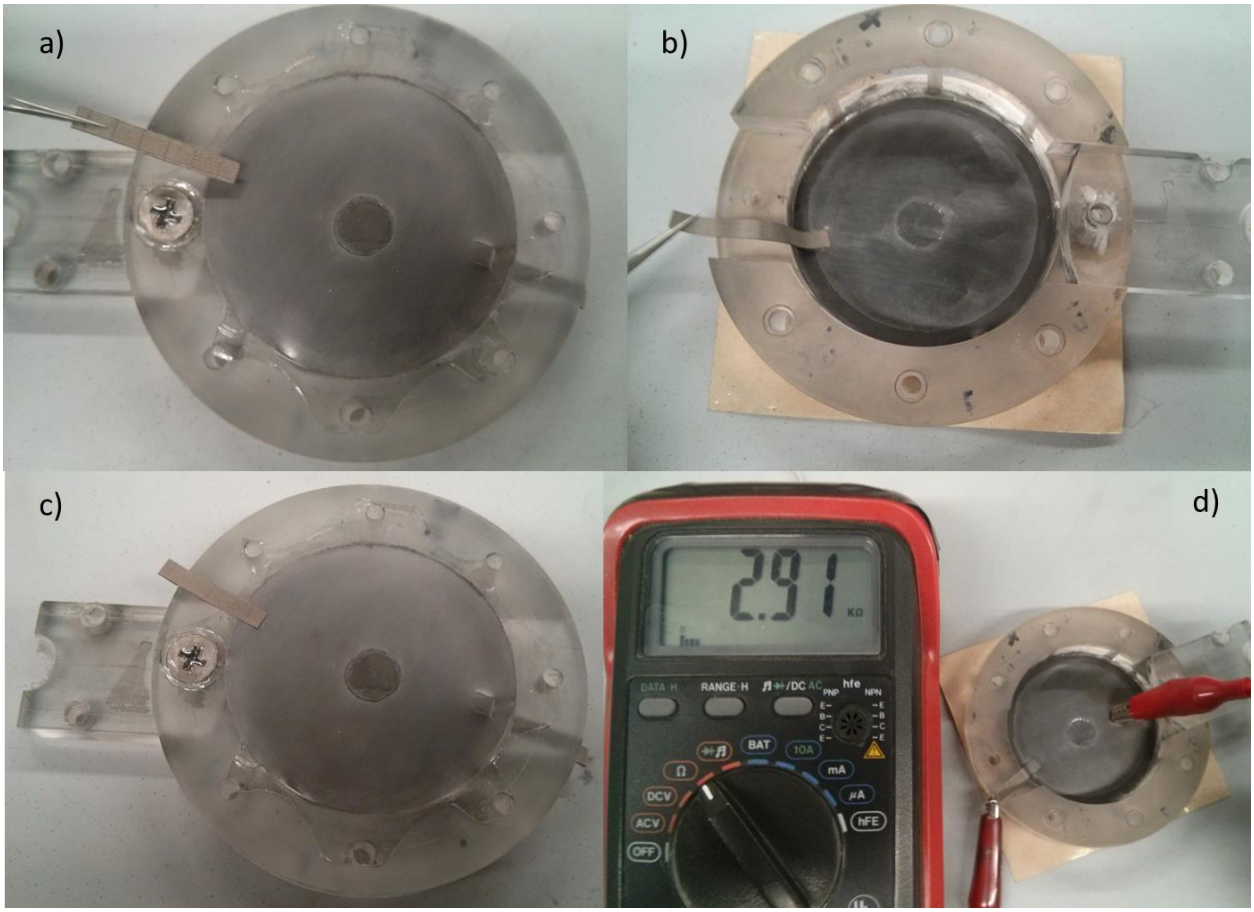

Figure 5-4: a) Top face electrical connection, b) bottom face electrical connection, c) completed actuator, d) resistance testing of the bottom electrode, showing 2.91kohm across the diameter

5.2 VARIABLE STIFFNESS STRUCTURE

The variable stiffness beam structure is a composite beam made up of two Ionomer-electrode layers between a pair of 0.127mm thick stainless steel layers of the same width as the Ionomer-electrode layers. Dimensions of the beam components are given below. A schematic of this structure is shown in Figure 5-5.

Figure 5-5: Schematic of the variable stiffness beam construction; (a) stainless steel shim outer layers, (b) Ionomer-electrode layers with bare electrode portions at oppsite ends of the beam

These stainless layers are used to adjust the composite or effective modulus of the beam in the passive state to match the actuator's elastic energy. If a beam with too low of a modulus is used, most or all of the deformation in the structure at equilibrium will be in the beam. If a beam with too high of a modulus is used, most or all of the deformation in the structure at equilibrium will be in the actuator. The goal of adjusting the effective modulus is to match or prescribe the deflection in the beam to the deflection in the actuator. This matching allows the equilibrium position and response of the structure to be tuned. A composite beam ready to be combined with the actuator is shown in Figure 5-6.

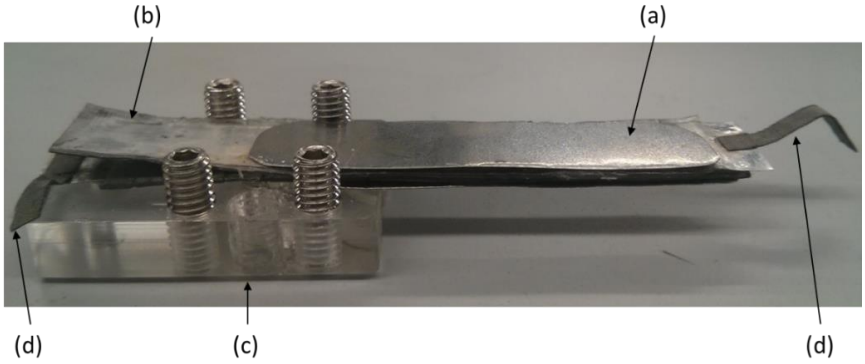

Figure 5-6: Variable stiffness composite beam; (a) upper stainless steel layer, (b) upper Ionomer-electrode layer, top clamp piece and hardware not shown for clarity (c) beam support portion of the test frame, (d) electrical connections

The Ionomer-electrode layers are fabricated by coating a strip of 0.02 mm thick aluminum electrode with the Ionomer solution using a draw-down bar film applicator. A photo of this process coating two electrodes at once is shown in Figure 5-7.

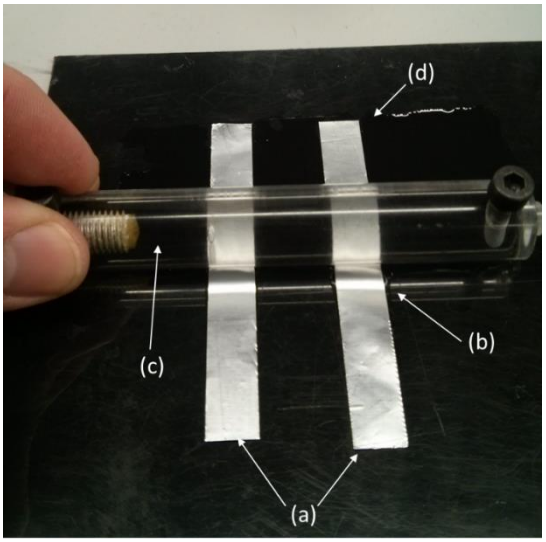

Figure 5-7: Draw down bar coating Ionomer on aluminum electrodes, direction of bar travel is toward the camera; (a) aluminum electrode layers, (b) meniscus of the bulk Ionomer material, (c) draw down bar, a polished acrylic cylinder in this case, (d) uniform film of Ionomer left behind the draw down bar

The sample is placed in a fume hood, letting the excess water evaporate until it has solidified. The excess Ionomer is trimmed off leaving a ½ to 1 mm border around the electrode. The coating and trimming process is then repeated for the other side of the electrode. This creates an Ionomer coating on both sides of the aluminum with one end left exposed for the electrical connection. The small border left around the electrode is to help prevent arcing between the layers once the beam is assembled. A schematic of the Ionomer-electrode layer construction is shown in Figure 5-8. Dimensions for the beam used in this work are 50mm coating length *a*, 12mm coating width *b*, 0.4mm completed thickness *t*.

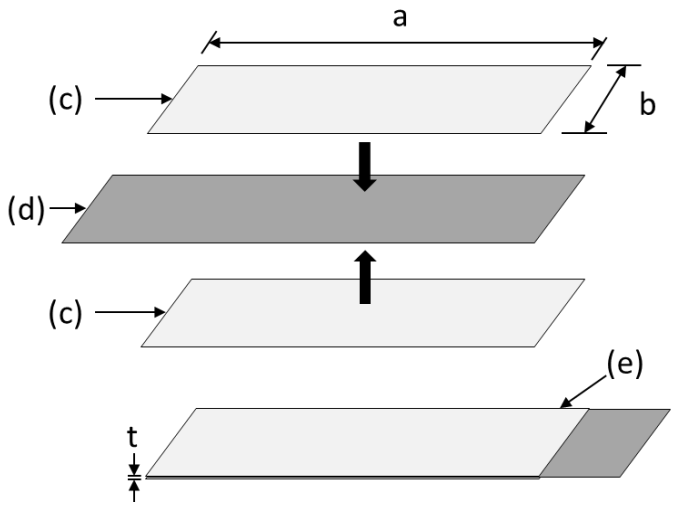

Figure 5-8: Schematic of Ionomer-electrode layer construction, dimensions for Ionomer coating length a and width b, completed thickness t; (c) ionomer layer, (d) aluminum electrode layer, (e) completed ionomer-electrode layer

Since both sides are coated, more layers may be added to increase the number of active interfaces in the structure. Three point bending tests of tri-layer beams (two interfaces) have shown close to double the change in effective elastic modulus compared to the two layer structure as mentioned in the background information. This indicates a proportional relationship between the number of layers or interfaces and the amount of change in the structure's effective modulus. For simplicity, this work focuses on beams composed of two layers only. A connection formed from a strip of CN-3910 tape is then adhered to the exposed aluminum layer. The two Ionomer-electrode layers are placed together with electric connections on opposite ends of the beam to prevent them from shorting. The Ionomer stack is then sandwiched between the stainless outer layers and one end is clamped in the test fixture. A completed morphing structure ready for testing is shown in Figure 5-9.

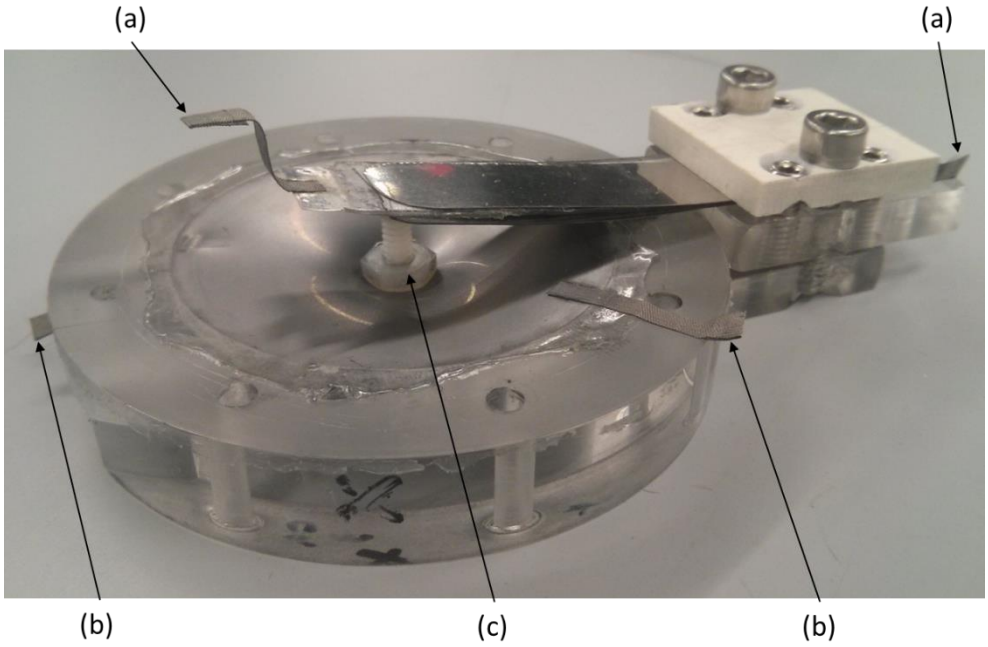

Figure 5-9: Assembled morphing structure used in this work; (a) variable stiffness beam power connections, (b) DEAP actuator power connections, (c) interface post coupling the beam to the actuator

6.0 EXPERIMENTAL METHOD

A simple test frame was fabricated from acrylic plastic and stainless steel hardware that allows the variable stiffness beam to be clamped at one end and held an adjustable distance from the actuator. This, along with the length of the interface post, allows control over the equilibrium state geometry parameters. Figure 6-1 shows the overall test instrumentation setup used for measurement and characterization of the morphing structure's response.

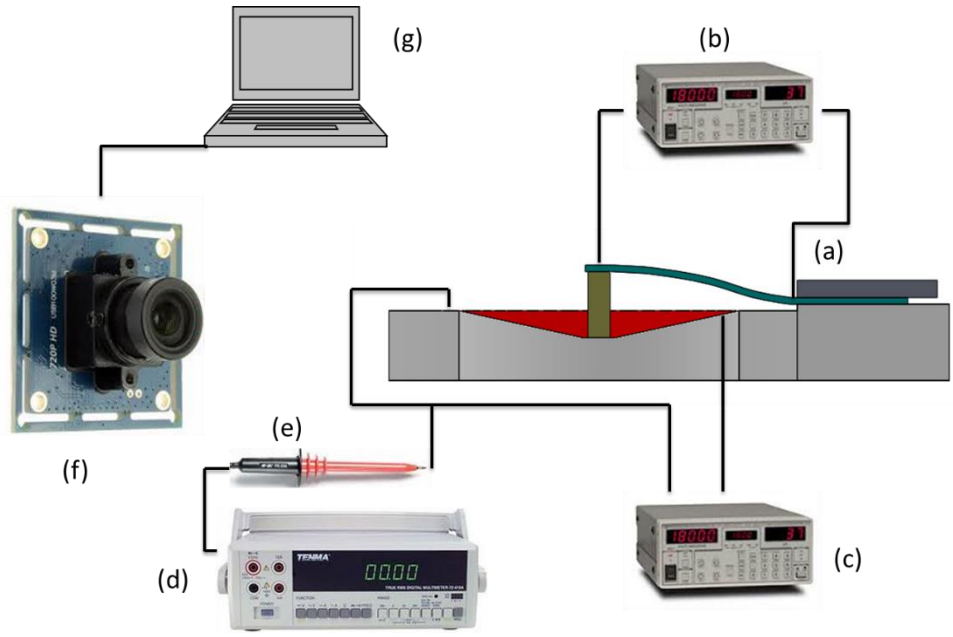

Figure 6-1: Schematic representation of the test setup; (a) morphing structure, (b) variable stiffness structure power supply, (c) actuator power supply, (d) multimeter, (e) 1000x high voltage probe, (f) USB camera, (g) PC with video capture and analysis software

6.1 ACTUATOR CONTROL SYSTEM

A high voltage power supply was built to provide driving voltage for the actuator. The supply is composed of a standard mains step down and rectification section, a variable frequency driver section and a high voltage fly-back transformer stage. The design is based on the work of Jean-Louis Naudin (Naudin, 2004). It is capable of providing variable output voltages from 0 to 10 kilovolts at a variable output frequency. The output voltage is monitored using a BK precision PR-28A 1000x high voltage probe connected to a Tenma 72-410A multimeter. Connections are made to the CN-3910 tape leads using high voltage silicone insulated wire and silicone insulated alligator clips.

6.2 VARIABLE STIFFNESS CONTROL SYSTEM

The variable stiffness structure is driven by a Stanford Research Systems PS325 power supply capable of up to 2500 volts at a maximum of 25 watts output. It provides a programmable over-current trip point and features an output current display with resolution to 0.01 milliamps. For the Ionomer materials and interface area of the beam used in this work, 500 volts is the maximum applied potential typically used. Connections are made to the CN-3910 tape leads with high voltage silicone insulated wire and silicone insulated alligator clips.

6.3 DISPLACEMENT MEASUREMENTS

Displacement of the variable stiffness beam during morphing tests was measured using a camera and video analysis software. Footage of the tests was captured by a computer connected to a USB camera with a 2.1mm lens and two megapixel CMOS detector at 1920x1080 pixel resolution and 30 frames per second. A ten millimeter scale bar was placed at approximately the same focal distance from the camera as the beam. The video of each test run was then analyzed using Tracker software (Douglas Brown, 2015). In the analysis, a virtual scale bar is matched to the physical one visible in the recording. The origin is placed at the frame supporting the actuator and the x-y axes are established. Each frame of the video is then reviewed and a target is placed on the pixel group corresponding to the beam tip. The multimeter readout corresponding to the actuator voltage is also visible in the frame. This allows actuator voltage versus displacement data to be collected for the structure. The displacement data is then extracted and tabulated by the software. In this work, the x-axis displacement is ignored as is the dynamic response of the structure. A screen capture of the Tracker software in use for this work is shown in Figure 6-2.

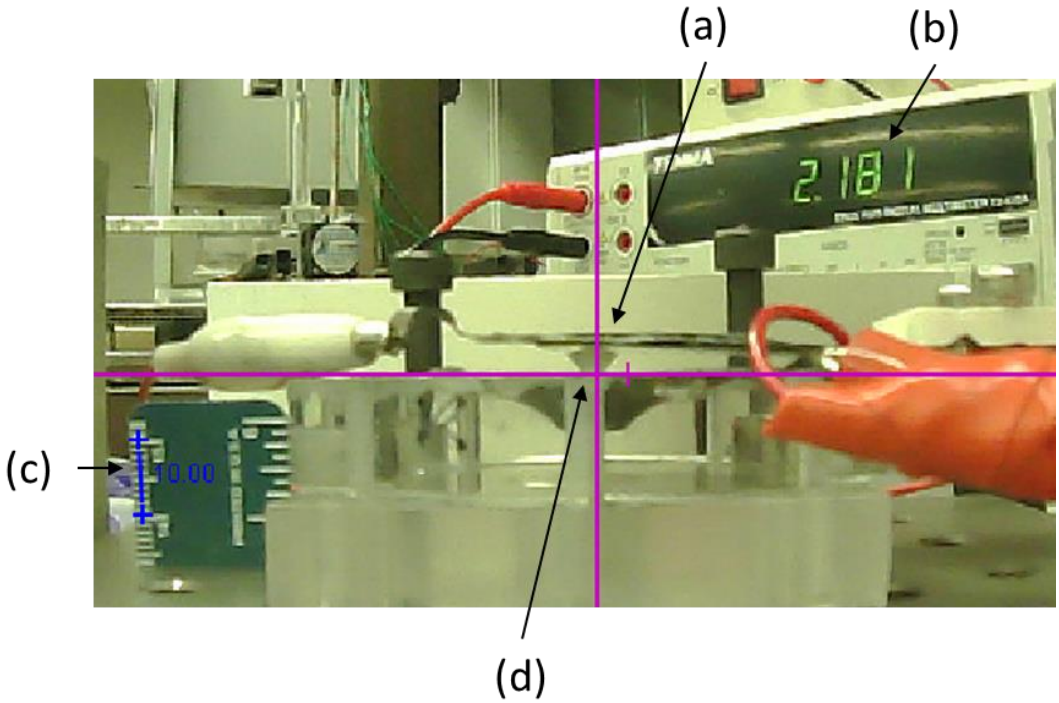

Figure 6-2: Annotated screen capture of Tracker software in use for morphing structure measurement; (a) variable stiffness beam, top edge is target for measurements, (b) measured actuator voltage, (c) 10mm scale bar over lay, (d) chosen origin and coordinate axes

The morphing structure is then placed on an aluminum breadboard to enable repeatable positioning and fixture locations. The breadboard is part of a linear motion stage, however, its motion capabilities are not used in this work. The power leads for both the actuator and variable stiffness structures are connected and the system is ready for testing. A photo in Figure 6-3 shows the breadboard setup with power leads connected.

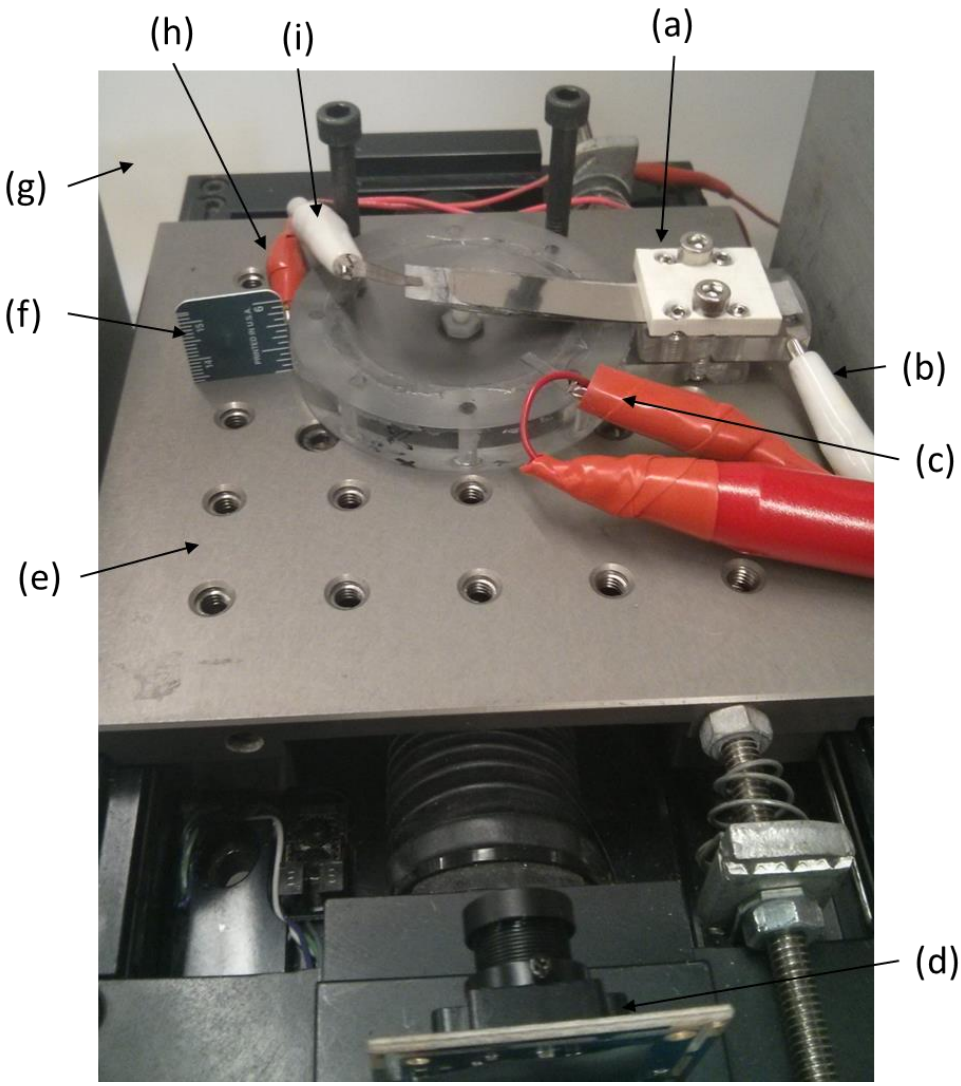

Figure 6-3: Annotated photo of the morphing structure and the measurement setup; (a) morphing structure being tested, (b) variable stiffness structure power connection, (c) actuator power connection and measurement probe, (d) USB camera for video capture, (e) bread board platform used as a base, (f) 10mm scale bar, (g) neutral backdrop to improve contrast in video images, (h) actuator power connection, (i) variable stiffness structure power connection

7.0 EXPERIMENTAL AND ANALYTICAL RESULTS

A series of experimental tests were performed to determine the performance of the morphing structure designed and constructed in this work. To complement these, several corresponding simulations using the analytical model developed in chapter 4 were performed.

Each test run was performed using the following general procedure. First, the actuator and variable stiffness beam are assembled in the test frame. This induces an initial displacement in both the actuator and the beam corresponding to the equilibrium position (state 2). The actuator control power supply is then activated and ramped to the target voltage of 3500 volts, allowing the actuator and beam to displace downwards. This corresponds to the beam going from a high tip deflection to a lower tip deflection, or straighter state. Once the actuated equilibrium state is reached, the variable stiffness beam is activated by applying -500 volts, thus switching it to the stiff state for the active morphing tests, or is left in the passive or soft state for the control tests. The actuator power supply is then turned off and the actuator displaces upwards, bending the beam back towards its initial deformed position. Once the hold state is reached, the test is concluded. A diagram of this cycle is shown in Figure 7-1.

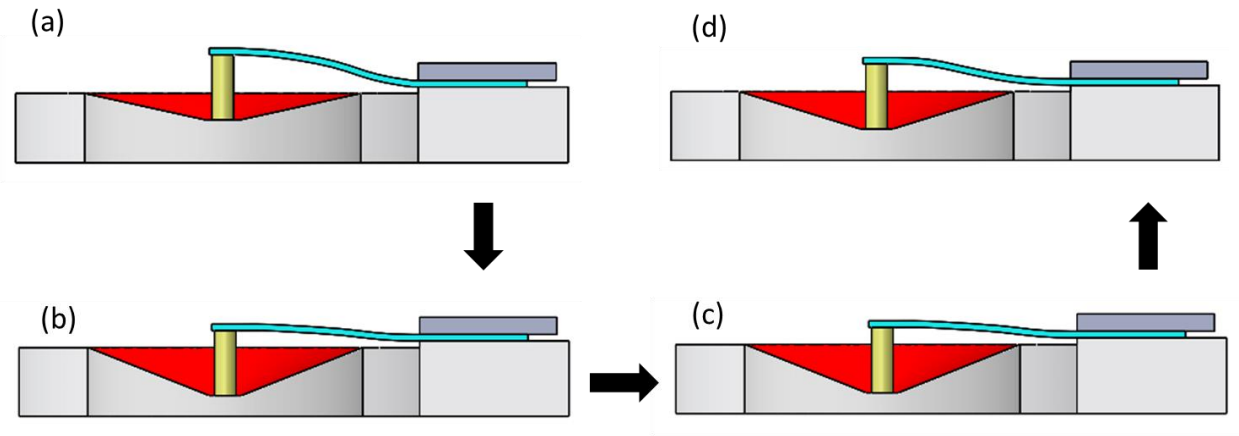

Figure 7-1: Sectioned view of morphing structure during a test run; (a) equilibrium, state 2, (b) actuated, state 3, (c) effective modulus variation and (d) hold, state 4

The parameter identified as a relative performance index is the hold distance. This distance corresponds to the change in position of the variable stiffness beam tip between the initial equilibrium position (state 2) and the final equilibrium position (state 4). A more absolute performance index is the hold percentage, defined as the hold distance as a percentage of the actuation distance from the initial equilibrium (state 2) to the actuated position (state 3). The hold percentage allows a more direct comparison of test results with different actuation distances due to variations in applied voltages to the actuator.

A phenomenon discovered during experimental testing is the issue of stiction or weak bonding between test runs. This arises in the variable stiffness structure not "resetting" to its passive or lower stiffness state when the electric voltage is removed. This is likely due to affinity between the two Ionomer layers after being pressed together and deformed. In order to reset the stiffness, one must separate the layers either by peeling them apart or slipping a thin piece of plastic between them. Potential means to address this will be presented in the following chapter. For now, we define "separation" tests as a test where the layers were separated prior to the test

and “no-separation” tests as a test where the layers were not separated prior to the test. In the no-separation tests, the number of previous test cycles performed without separation is also tracked. Test runs were conducted with active and control tests taking place in the same group of tests. For the no separation tests, the group of tests the data was collected in is represented by the letter before the cycles post separation value in the x-axis.

Control tests only use the state of the Ionomer power supply as the control variable as the layers may have been charged in the previous test. While there is a discharge time period for the Johnsen-Rahbek effect, the length of time between tests is long enough to negate residual charge effects.

7.1 EXPERIMENTAL MORPHING DATA

The tests performed for the morphing active data represent the non-control data sets. In these tests, the variable stiffness beam was cycled from passive (soft) to active (stiff) at the actuated state equilibrium to demonstrate the shape morphing capability of the structure.

7.1.1 Separation tests

The total deflection, or the distance between the equilibrium and actuated states and the hold distance, or distance between the equilibrium and hold states from the separation tests is shown graphically in Figure 7-2. These correspond to the “Displacement” and “Hold” distances defined in Figure 1-1. Each bar corresponds to a single test run and the error bars correspond to

plus or minus one standard error calculated for the entire measured data set of the tests shown. The raw data and the calculated hold percentages are shown in Table 7-1.

The total deflection is calculated as the difference in equilibrium and actuated positions and the hold distance is calculated as the difference in equilibrium and final positions. The hold percentage is simply the hold distance as a percentage of the total deflection distance.

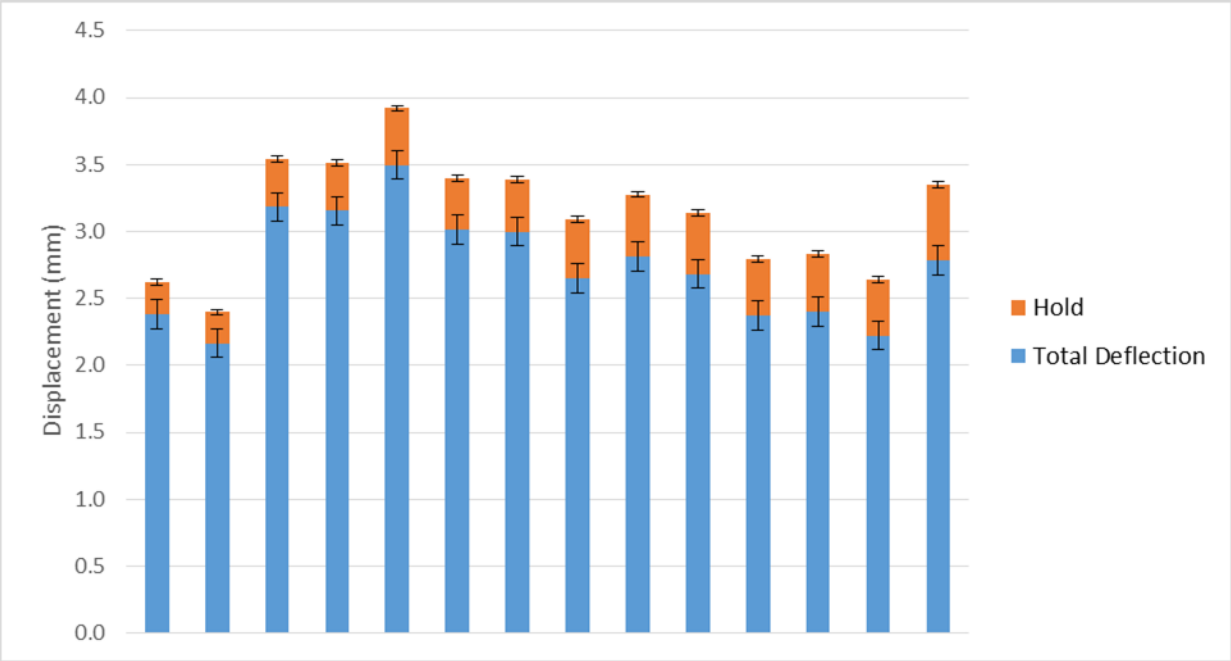

Figure 7-2: Active shape morphing data with separation of the variable stiffness layers performed between tests

Table 7-1: Tabulated measurements of active shape morphing tests and calculated hold percentage of total deflection

Equilibrium [mm]	Final [mm]	Actuated [mm]	Total deflection [mm]	Hold [mm]	Hold [%]
8.663	8.422	6.282	2.381	0.241	10.1
8.452	8.220	6.287	2.165	0.232	10.7
6.180	5.823	2.998	3.182	0.356	11.2
8.852	8.498	5.697	3.155	0.355	11.2
6.375	5.951	2.879	3.496	0.424	12.1
9.185	8.805	6.170	3.015	0.380	12.6
9.146	8.754	6.147	2.999	0.392	13.1
6.644	6.208	3.992	2.652	0.436	16.4
8.648	8.182	5.835	2.813	0.465	16.5
7.872	7.413	5.190	2.682	0.459	17.1
8.893	8.467	6.521	2.372	0.426	18.0
6.701	6.269	4.298	2.403	0.432	18.0
6.581	6.160	4.360	2.221	0.421	18.9
9.065	8.501	6.282	2.783	0.564	20.3

From this data, we can report a mean hold percentage of 14.7% with a 95% confidence interval of ± 1.86%.

7.1.2 No Separation tests

The total deflection, or the distance between the equilibrium and actuated states and the hold distance, or distance between the equilibrium and hold states from the separation tests is shown graphically in Figure 7-3. Each bar corresponds to a single test run and the error bars correspond to plus or minus one standard error calculated for the entire measured data set of the tests shown. The horizontal axis indicates “cycles post-separation” for each test, which indicates for the data point shown, how many test cycles had been run since the last separation of beam layers. The raw data and the calculated hold percentage are shown in Table 7-2. Note the first

three tests show the behavior of a failure to reset the variable stiffness structure that was mentioned earlier in the chapter. That is, in cycles 2 and 3, there is lower total deflection than in cycle 1, and no measurable hold at the end of the cycle. This would suggest that during the second and third cycles, the beam layers are still bonded from the first cycle, and the beam remains in its high stiffness state. The apparent lack of the behavior in the subsequent tests will be addressed in the following chapter.

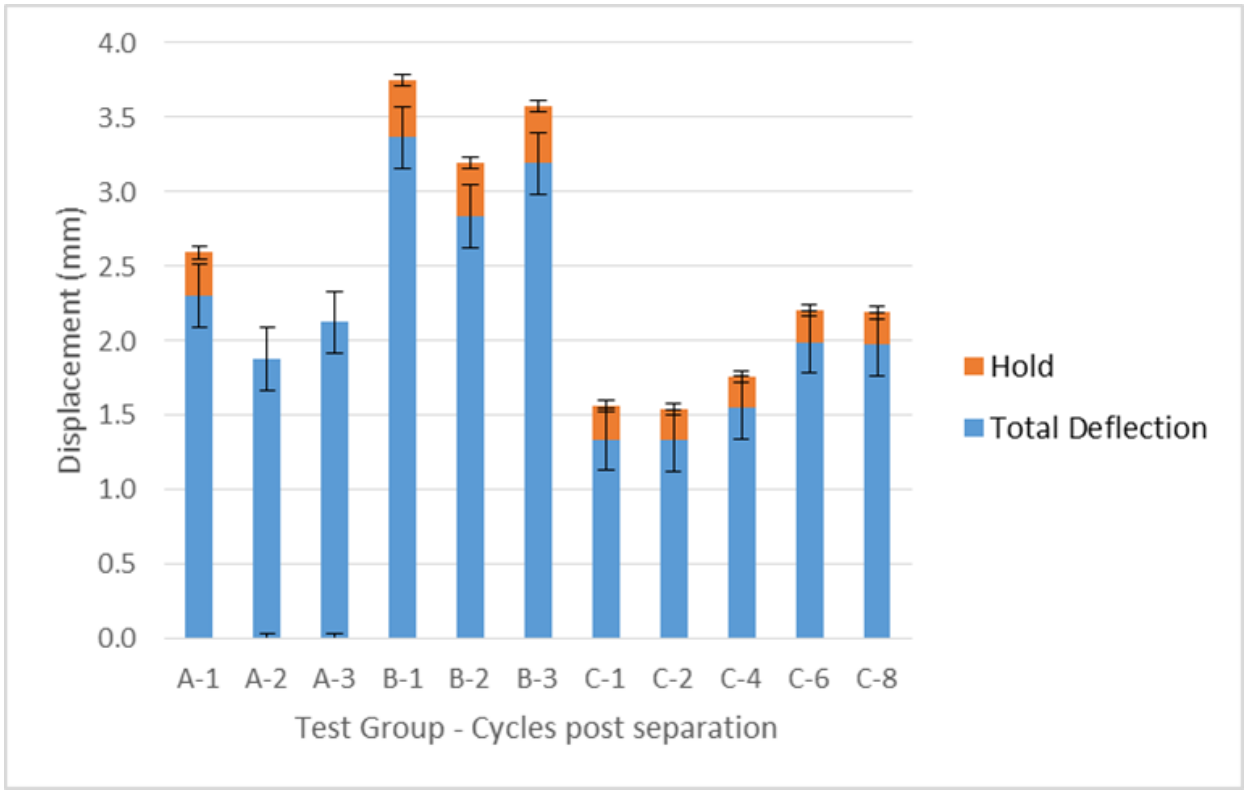

Figure 7-3: Active shape morphing data without separation of the variable stiffness layers between tests

Table 7-2: Tabulated measurements of active shape morphing tests and calculated hold percentage of total deflection for no separation tests

Equilibrium [mm]	Final [mm]	Actuated [mm]	Total deflection [mm]	Hold [mm]	Hold [%]	Cycles post separation
8.497	8.208	6.197	2.300	0.289	12.6	1
8.256	8.265	6.378	1.879	-0.009	-0.5	2
8.365	8.375	6.244	2.122	-0.010	-0.4	3
6.081	5.696	2.717	3.364	0.385	11.5	1
5.937	5.579	3.100	2.837	0.357	12.6	2
5.859	5.477	2.670	3.189	0.383	12.0	3
6.934	6.713	5.597	1.337	0.222	16.6	1
6.569	6.359	5.242	1.328	0.210	15.8	2
6.409	6.201	4.860	1.550	0.208	13.4	4
6.506	6.295	4.516	1.990	0.212	10.6	6
6.319	6.103	4.348	1.971	0.217	11.0	8

From this data, we can report a mean hold percentage of 10.5% with a 95% confidence interval of ± 3.44%.

7.2 EXPERIMENTAL CONTROL DATA

Throughout testing, control tests were performed to identify the effect of any other phenomena on the hold distance/percentage aside from the application of electrical potential to the variable stiffness structure. These were performed in the same manner as the active tests with the only difference being the variable stiffness power supply remained off throughout the test run.

7.2.1 Control Separation tests

The total deflection, or the distance between the equilibrium and actuated states and the hold distance, or distance between the equilibrium and hold states from the control separation tests is shown graphically in Figure 7-4. Each bar corresponds to a single test run and the error bars correspond to plus or minus one standard error calculated for the entire measured data set of the tests shown. The raw data and the calculated hold percentage are shown in Table 7-3. A statistically significant and somewhat consistent hold percentage is apparent in the data despite being from control tests. This suggests the presence of another source aside from stiffness variation contributing to the measured hold percentage.

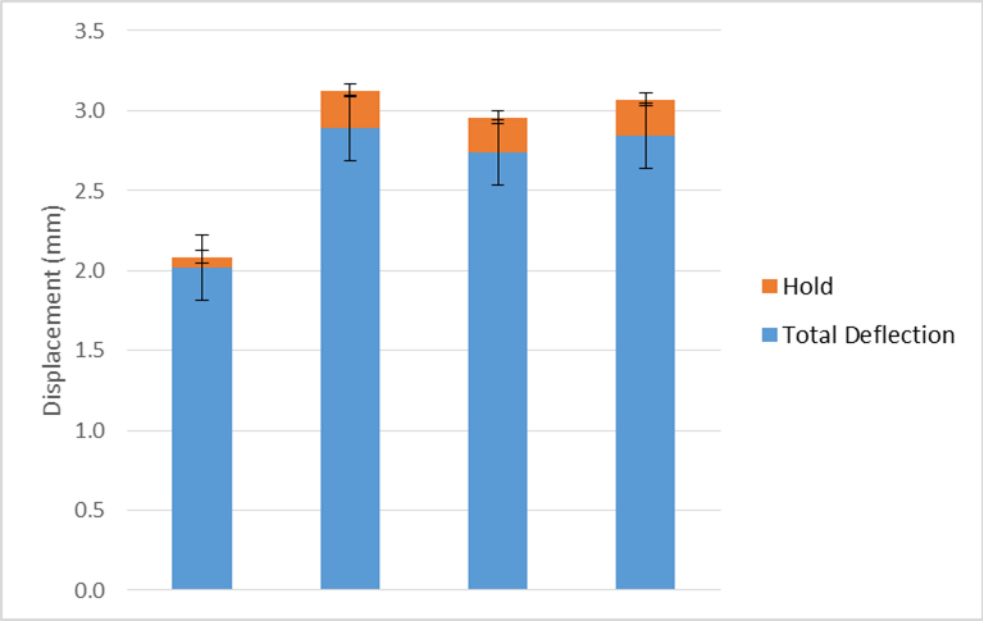

Figure 7-4: Control data with separation of the variable stiffness layers performed between tests

Table 7-3: Tabulated measurements of control tests and calculated hold percentage of total deflection for separation tests

Equilibrium [mm]	Final [mm]	Actuated [mm]	Total deflection [mm]	Hold [mm]	Hold [%]
10.950	10.883	8.935	2.015	0.067	3.3
8.904	8.669	6.013	2.891	0.235	8.1
8.665	8.449	5.924	2.741	0.216	7.9
8.837	8.613	5.992	2.845	0.225	7.9

From this data, we can report a mean hold percentage of 6.8% with a 95% confidence interval of ± 2.33%. While this hold percentage is present, the mean is still less than half of that for the active tests with separation between runs.

7.2.2 Control No Separation tests

The total deflection, or the distance between the equilibrium and actuated states and the hold distance, or distance between the equilibrium and hold states from the separation tests is shown graphically in Figure 7-5. Each bar corresponds to a single test run and the error bars correspond to plus or minus one standard error calculated for the entire measured data set of the tests shown. The horizontal axis indicates cycles post-separation values for each test. The raw data and the calculated hold percentage are shown in Table 7-4. Note the first three tests show the expected behavior of a control test. That is, in cycles 4, 5 and 6 from test group A, there is no significant hold at the end of each test. This would initially suggest that the hold percentage observed in the separated tests is related to the layers being peeled apart or separated. However, the observation of a similar hold percentage as that of the separated control tests in the next two

tests from test group B indicates the source is related to the test group the run is from. This would indicate a relation of loading history and prior tests to the hold percentage observed.

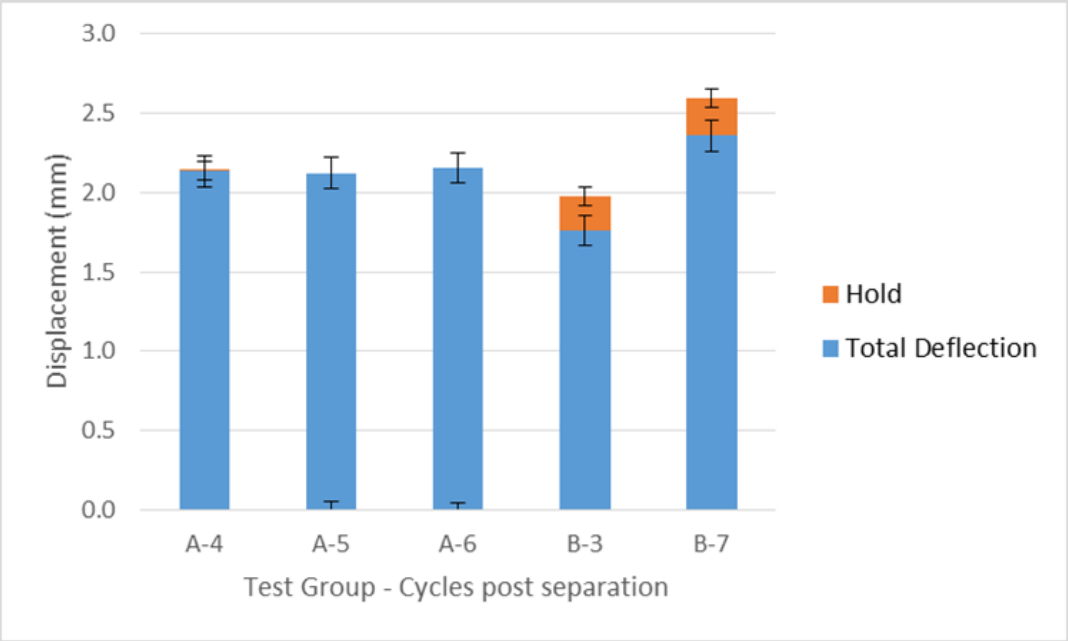

Figure 7-5: Control data without separation of the variable stiffness layers performed between tests

Table 7-4: Tabulated measurements of control tests and calculated hold percentage of total deflection for no separation tests

Equilibrium [mm]	Final [mm]	Actuated [mm]	Total deflection [mm]	Hold [mm]	Hold [%]	Cycles post separation
8.064	8.064	5.928	2.136	0.000	0.0	4
8.370	8.374	6.246	2.124	-0.004	-0.2	5
8.251	8.259	6.094	2.157	-0.008	-0.4	6
6.625	6.408	4.863	1.761	0.217	12.3	3
6.678	6.443	4.319	2.359	0.235	9.9	7

From this data, we can report a mean hold percentage of 3.4% with a 95% confidence interval of ± 5.59%.

7.3 ANALYTICAL SIMULATIONS

7.3.1 Active morphing simulations

In the active morphing simulations, a MATLAB script based on the analytical model developed in chapter 4 is used. Simulations with the *k*, or effective modulus multiplication factor set to 1.4, corresponding to the experimentally determined *k* factor for the variable stiffness beam in cantilever loading were performed, varying the value of the fabrication state principal radial stretch. This shows the effect of the fabrication state principal stretches on the actuator's deflection versus applied voltage performance. A second set of simulations was performed with the principal radial stretch set to 4 and the *k* factor varied to show its effect on the hold percentage achieved. The simulation results are shown graphically in Figure 7-6 and Figure 7-7. The raw data from the simulations is shown in Table 7-5. The tests in Figure 7-6 and the first three rows of Table 7-5 show the expected trend of decreasing actuation deflection and a corresponding decrease in hold distance as the hold percentage is held constant due to *k* being fixed at a constant value. This illustrates the effect of higher stress states due to larger principal stretches in the actuator on the deflection and hold distances. Figure 7-7 and the last four rows of Table 7-5 show the effect of the stiffness variation on the hold distance and percentage. Due to constant stress from the principal stretches, the actuation deflection is constant and the hold percentage decreases with lower values of *k*.

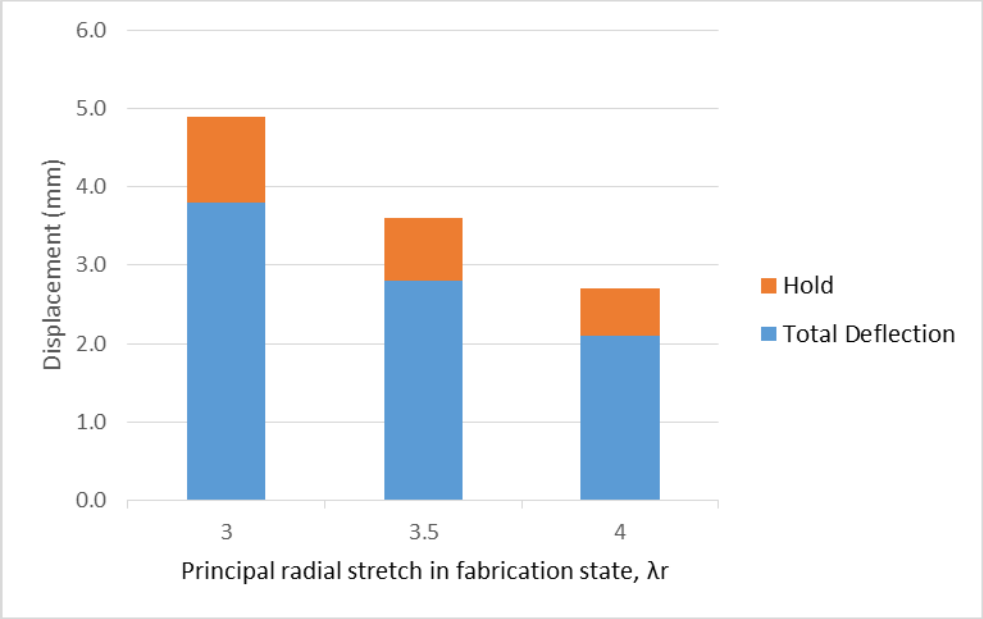

Figure 7-6: Analytical simulation for active morphing using a *k* factor of 1.4

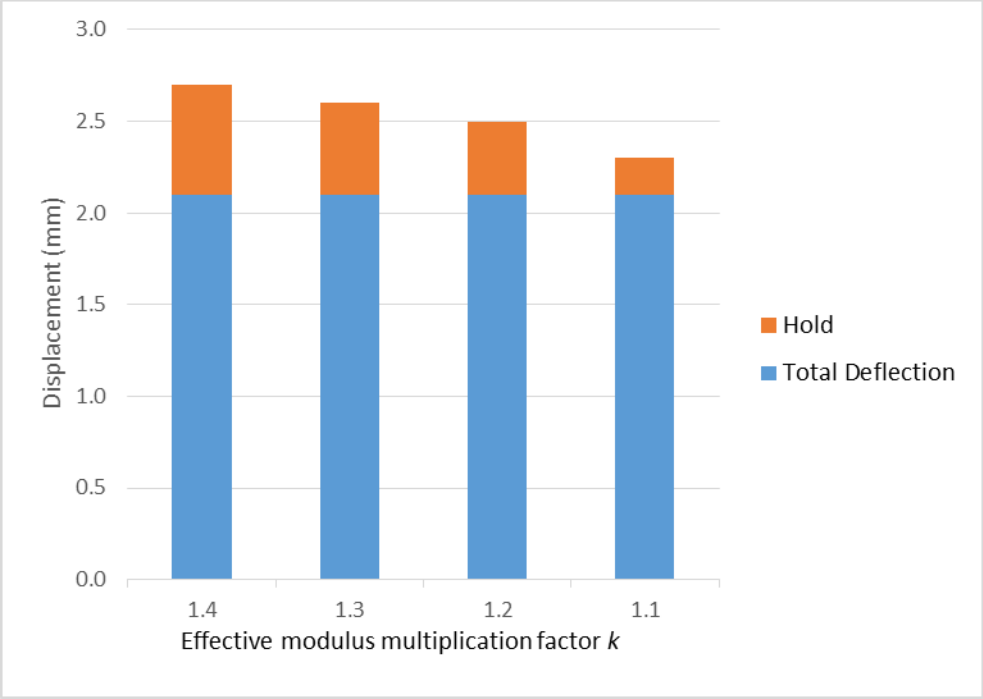

Figure 7-7: Analytical simulation for active morphing using a λ_r value of 4

Table 7-5: Active morphing analytical data

Equilibrium [mm]	Final [mm]	Actuated [mm]	Total deflection [mm]	Hold [mm]	Hold [%]	Fabrication state λ_r	Modulus factor *k*
5.956	4.856	2.156	3.800	1.100	28.9	3	1.4
6.756	5.956	3.956	2.800	0.800	28.6	3.5	1.4
7.456	6.856	5.356	2.100	0.600	28.6	4	1.4
7.456	6.956	5.356	2.100	0.500	23.8	4	1.3
7.456	7.056	5.356	2.100	0.400	19.0	4	1.2
7.456	7.256	5.356	2.100	0.200	9.5	4	1.1

7.3.2 Control simulations

Control simulations were performed using a *k* factor of 1 and varying the value of the fabrication state principal radial stretch. The simulation results are shown graphically in Figure 7-8 and the raw data is shown in Table 7-6. Similar to the active simulation data for variation of principal stretches, the actuation deflection decreases with increasing stretches and higher stress state in the actuator. As expected for a *k* value of 1, there is no hold predicted by the model.

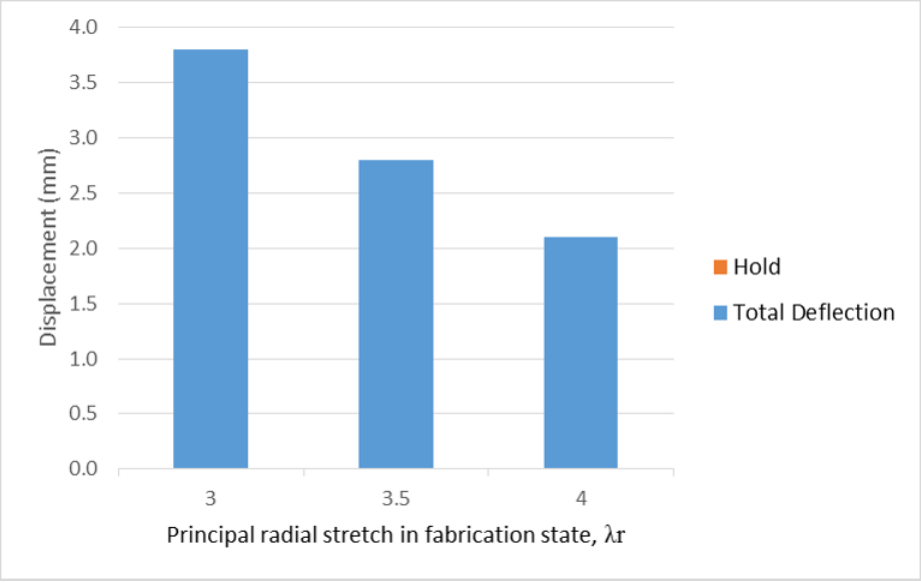

Figure 7-8: Analytical control simulation using a k factor of 1

Table 7-6: Analytical control data

Equilibrium [mm]	Final [mm]	Actuated [mm]	Total deflection [mm]	Hold [mm]	Hold [%]	Fabrication state λ_r
5.956	5.956	2.156	3.800	0.000	0.0	3
6.756	6.756	3.956	2.800	0.000	0.0	3.5
7.456	7.456	5.356	2.100	0.000	0.0	4

8.0 DISCUSSION

In this work, we have demonstrated a functional shape morphing structure design and experimentally determined its performance. An analytical model was developed to predict the response and performance parameters of this and shape morphing structures of a similar design.

One major issue observed in the structure as tested is the failure of the variable stiffness structure to reset to the lower stiffness state when the voltage is removed. This is likely due to the boundary conditions imposed by the cantilever loading and the amount of deflection experienced by the beam. As the layers are rigidly constrained together at one end in cantilever loading, the relative motion between the layers needed to release the bond is not possible. Theoretically, the bond caused by the Johnsen-Rahbek effect should disappear after a short discharge time period once the voltage is removed. One explanation for the continued bond is that the Ionomer behaves as most soft polymers and has an affinity for similar materials. The two layers are pressed together by the composite beam construction and the deflection process further wrings the surfaces together, causing a weak surface-to-surface bond to form in the interface. We have shown through experimental control testing that this weak bond is not responsible for the stiffness variation effect. This behavior is obvious in the first three no separation tests performed. The first test behaves as expected but no hold or morphing is apparent in the subsequent two tests as the weak bond has prevented a change in stiffness from occurring. This behavior is not apparent in all no-separation tests, however, as subsequent no-separation tests show non-zero

hold distances and morphing. While this alone could be taken to be an indication of the variable stiffness structure resetting properly, comparison with the no separation control data and most of the separation test data show similar hold distances and morphing despite not having any voltage applied. This is likely due to viscoelastic effects in the actuator and stress relaxation due to time spent in the actuated state and the number of cycles. Due to the presence of a significant hold percentage in control tests, it's likely a similar percentage of hold in the active tests is due to the same cause while the remaining percentage is due to stiffness variation. The feasibility of functional shape morphing devices using Ionomer-based variable modulus structures will be dependent on finding a working solution to the stiffness reset issue.

8.1 EXPERIMENTAL VERSUS ANALYTICAL RESULTS

As mentioned in section 3.2, the experimentally determined maximum performance for the variable stiffness structure used corresponds to an effective modulus multiplication factor, *k*, of 1.4 and the ideal case of variation between a frictionless two layer beam and an ideally bonded two layer beam corresponds to a *k* of 4 as shown in Figure 3-7. From the analytical simulations, a *k* value of 1.4 corresponds to a hold of about 29 percent as shown in Table 7-5 and a *k* value of 4 corresponds to a hold of 75 percent. From the experimental testing, the mean hold from the separation tests was about 14 percent. Comparing the simulation data in Table 7-5 for the *k* factor variation, it's likely the *k* factor observed in the experimental morphing tests is actually somewhere between 1.1 and 1.2. The large amount of noise and lower force readings observed in the cantilever beam bending versus the three-point tests indicate the forces may be at the lower limit of the measurable range of the load cell.

The simulated control data failed to predict the hold percentages shown in the experimental control tests. As this behavior in the experimental data is likely a function of the viscoelastic response and load history of the actuator prior to that test and the model does not take these into account, the discrepancy is to be expected. Taking the hold percentage assumed due to viscoelastic effects observed in the control data and subtracting it from the active data, the residual hold from the variable stiffness structure is approximately 8 percent.

One property of the Ionomer not previously mentioned is the dependence of its modulus and the mobility of the tetramethylammonium ion on water content. As the Ionomer is water swelling, an increase in water content results in a lower modulus and higher ion mobility. Rudimentary control of the humidity for sample storage was used to prevent large changes in water content. As the exact water content is not known for each test, variations in the actual modulus of the Ionomer are a possibility.

8.2 FUTURE WORK

In the course of the research and testing performed for this work, several areas for future work were identified as significant for improving shape morphing structure design and performance.

Improvement in the ability of the variable stiffness structure to reset is likely the most important goal of any future design using a structure similar to the one used here. We have identified two promising paths for solving this issue. The first is through doping or morphology control of the interface surfaces of the Ionomer layers. As the Johnsen-Rahbek effect relies on the surface roughness in the contact layer to create the small dielectric volumes for electrostatic forces to occur in, a surface doping of a dielectric into these voids could allow lower interfacial

friction by preventing the surfaces from wringing together. Friction could also be reduced by the lubricity of the material used in the doping. If the doping is carried out in a manner that minimizes the reduction in the Johnsen-Rahbek effect, a higher delta in the stiffness variation should be achieved in addition to the ability for the structure to reset.

The second path for the variable stiffness resetting is the boundary conditions used in loading the structure. The use of compliant supports and large enough deflections may allow the layers to move enough with respect to each other to break the weak bond between them. Potentially, an antagonistic actuator may be useful in resetting the structure as well as allowing for actuation and morphing in two directions from equilibrium.

A second area important for future work is the use of three or more layers in the Ionomer structure or potentially a different form of an Ionomer-based variable stiffness structure. More layers in the Ionomer structure have demonstrated a proportional increase in the variation of the stiffness. A structure with a larger stiffness delta or higher k factor should be capable of larger hold percentages than the two layer structure used here. Other forms of a variable stiffness structures are possible using the Ionomer and some very interesting designs have been proposed recently. A more accurate and complete set of material models and k factors and their dependence on water content for the Ionomer structure would greatly improve the accuracy of the results from any simulations. An in-depth study of the material properties should be considered as a vital step in any future research in variable stiffness structures using this material.

The third area for future research is to improve the modeling and control of the morphing structure. The expansion of the system model to predict dynamic response and account for the viscoelastic nature of the actuator material more accurately will be important for many potential

applications. Tests quantifying the effect of the viscoelastic response on the hold distances should be performed to improve the model's predictions and account for the hold distances observed in the control tests. The modification of the system model to use a shear-inclusive beam theory would also improve the accuracy of the analytical results. However this will be dependent on the accuracy of the material parameters determined for the composite beam. A larger goal for improvement of the model would be to incorporate forward and inverse morphing algorithms such as the one developed by Motlagh in his work with morphing structures. This could provide a robust predictive model for the morphing response and thus determine appropriate voltages for the actuator and variable stiffness structure in order to morph into a selected shape.

APPENDIX A

MATLAB IMPLEMENTATION OF THE ANALYTICAL MODEL

File: Morphing_model.m

```
%% Diaphragm Dielectric electro-active polymer actuator (DEAP) and Ionomer
variable stiffness cantilever beam morphing structure
%%Calculates equilibrium, actuated and hold positions for a given
actuator/beam configuration
%Uses 3 parameter Ogden formulation for hyperelastic materials

%Created by Eliot George, 2/25/2015
%M.S Thesis, Mechanical Engineering, University of Pittsburgh

%% Initial un-stretched elastomer at rest State (0)
r0=0.0127; %(m) Initial Elastomer radius (un-stretched) 0.5"
z0=0.000508; %(m) Initial Elastomer thickness (un-stretched) 0.020"

%% Actuator Fabrication State (1)
r1=0.0254; %(m) Fabricated Elastomer radius (stretched) 1.125"
z1=0.0000254; %LamzF*z0 %Fabricated Elastomer thickness (stretched) measured,
also by incompressible material condition (LamrF*LamcF*LamzF=1) & LamzF=z1/z0
LamrF=4; % Fabrication radial stretch in cylindrical Coords
LamcF=4; % Fabrication circumferential stretch in cylindrical Coords
LamzF=1/(LamrF*LamcF); % 1/20= Fabrication thickness stretch in cylindrical
Coords

area1t=pi*r1^2; %(m^2) Fabrication state total surface area
vol1t=area1t*z1; %(m^3) Fabrication state total volume

rin=0.003; %inner fixed disk radius
L1=0.0224; %active length 2" diameter, 6mm center
area1=pi*(L1+rin)^2-pi*rin^2;  %(m^2) Fabrication state (active) surface area
vol1=area1*z1; %(m^3) Fabrication state active volume

%% Actuator Equilibrium State (2)
interface=0.0109855; %(m) Interface post length
offset=0.00127; %(m) Beam offset from actuator surface plane
```

```
syms d2

L2=sqrt(L1^2+d2^2); %d2=sqrt(r2^2-r1^2); %Pythagorean theorem for equilibrium
relation, d2 is equilibrium displacement
LamrE=L2/L1; % Equilibrium radial stretch in cylindrical Coords
LamcE=1; % Equilibrium circumferential stretch in cylindrical Coords
LamzE=1/(LamrE*LamcE); % Equilibrium thickness stretch in cylindrical CoordsE
z2=LamzE*z1; % Equilibrium Elastomer thickness (stretched)

Sigmar2=LPPsiOGsum( LamrE, LamrF )- LPPsiOGsum( LamzE, LamzF );
Sigmar2=simplify(Sigmar2);

y2=interface-offset-d2;

%% Morphing Structure Equilibrium (2) Geometry and Constraints

%Beam material Properties
E=522000000; % beam passive state effective elastic modulus

Fbeam2=ForceBeam( E, y2 );
Fbeam2=simplify(Fbeam2);
Factuator2=ForceActuator( z2, d2, Sigmar2 );
Factuator2=simplify(Factuator2);

d2sym=solve(Fbeam2==Factuator2, d2);
d2s=double(d2sym)

L2=sqrt(L1^2+d2s^2);
y2=interface-offset-d2s;
LamrE=L2/L1; % Equilibrium radial stretch in cylindrical Coords
LamcE=1; % Equilibrium circumferential stretch in cylindrical Coords
LamzE=1/(LamrE*LamcE); % Equilibrium thickness stretch in cylindrical CoordsE
z2=LamzE*z1; % Equilibrium Elastomer thickness (stretched)
y2=interface-offset-d2s;
Fbeam2=ForceBeam( E, y2 );

%% Actuated state (3)

syms d3
L3=sqrt(L1^2+d3^2); %d2=sqrt(r2^2-r1^2); %Pythagorean theorem for equilibrium
relation, d2 is equilibrium displacement
LamrA=L3/L2; % Equilibrium radial stretch in cylindrical Coords
LamcA=1; % Equilibrium circumferential stretch in cylindrical Coords
LamzA=1/(LamrA*LamcA); % Equilibrium thickness stretch in cylindrical CoordsE
z3=LamzA*z2;

y3=interface-offset-d3;

%Maxwell stress during actuation
Phi=3500;
sigmA=Maxwell( Phi, z3 );

%Elastic stress during actuation
```

```
Sigmar3=LPPsiOGsum( LamrA, LamrE*LamrF )- LPPsiOGsum( LamzA, LamzE*LamzF );
Sigmar3=simplify(Sigmar3);
Sigmar3total=Sigmar3-sigmA;
Sigmar3total=simplify(Sigmar3total);

Fbeam3=ForceBeam( E, y3 );
Fbeam3=simplify(Fbeam3);
Factuator3=ForceActuator( z3, d3, Sigmar3total );
Factuator3=simplify(Factuator3);

d3sym=solve(Fbeam3==Factuator3, d3);
d3s=double(d3sym)

delta=d3s-d2s

L3=sqrt(L1^2+d3s^2); %d2=sqrt(r2^2-r1^2); %Pythagorean theorem for
equilibrium relation, d2 is equilibrium displacement
LamrA=L3/L2; % Equilibrium radial stretch in cylindrical Coords
LamcA=1; % Equilibrium circumferential stretch in cylindrical Coords
LamzA=1/(LamrA*LamcA); % Equilibrium thickness stretch in cylindrical CoordsE
z3=LamzA*z2;
y3=interface-offset-d3s;
Fbeam3=ForceBeam( E, y3 );
%% Ionomer activation
Eon=1.4*E;

%% Relaxation and spring-back state (4)

%Beam geometry
b=0.01143; %(m) Beam Width
h=0.0010668; %(m) Beam Thickness
l=0.040; %(m) Beam Length
I=(b*h^3)/12; %(m^4) Beam second moment of area

deltay=((Fbeam2-Fbeam3)*(l^3))/(3*Eon*I);
y4=y3+deltay;
d4=interface-offset-y4

delta2=d4-d3s
hold=d4-d2s
```

File: LPPsiOGsum.m

```
function [ LamParPsi] = LPPsiOGsum( Lam1, Lam2 )
%UNTITLED3 Summary of this function goes here
%   Detailed explanation goes here
mu=[8580, 84300, -023300];
alpha=[1.293, 2.3252, 2.561];

LamParPsi=mu(1)*(Lam1^alpha(1))*(Lam2^alpha(1))+mu(2)*(Lam1^alpha(2))*(Lam2^a
lpha(2))+mu(3)*(Lam1^alpha(3))*(Lam2^alpha(3));
 end
```

File: ForceBeam.m

```
function [ Fbeam ] = ForceBeam( E, y )
%calculates force for cantilever beam bending
%   determines reaction force for given stiffness and deflection for a
%   pre-determined cross-section and length.

%Beam geometry
b=0.01143; %(m) Beam Width
h=0.0010668; %(m) Beam Thickness
l=0.040; %(m) Beam Length
I=(b*h^3)/12; %(m^4) Beam second moment of area

Fbeam=(3*E*I*y)/(l^3); %Equilibrium reaction force

end
```

File: ForceActuator.m

```
function [ Factuator ] = ForceActuator( z, d, Sigmar )
%calculates axial force in the DEAP diaphragm acutator for a given stretch,
%thickness and radial stress value

csA=pi*0.006*z;

L1=0.0224; %active length 2" diameter, 6mm center

L=sqrt(L1^2+d^2);

sintheta=(d/L)*(1+(d/L)^2)^(-1/2);

Fd=Sigmar*csA;

Factuator=Fd*sintheta;

end
```

File: Maxwell.m

```
function [ SigmaM ] = Maxwell( V, z)
%Calculates the Maxwell stress or eletrostatic pressure for a given voltage
%and electrode seperation distance.

%%Electric constants

er=4.7; %F/m relative permitivity, dielectric constant e=er/e0
e0=0.00000000000885; %F/m Vacuum permitivity

%%Maxwell stress during actuation
SigmaM=er*e0*(V/z)^2;

end
```

APPENDIX B

ACTUATOR RESPONSE CURVES

Actuator voltage vs displacement curves are shown in Figure B-1 and Figure B-2. In Figure B-2, three tests were performed successively to demonstrate the viscoelastic relaxation and fading memory in the actuator material.

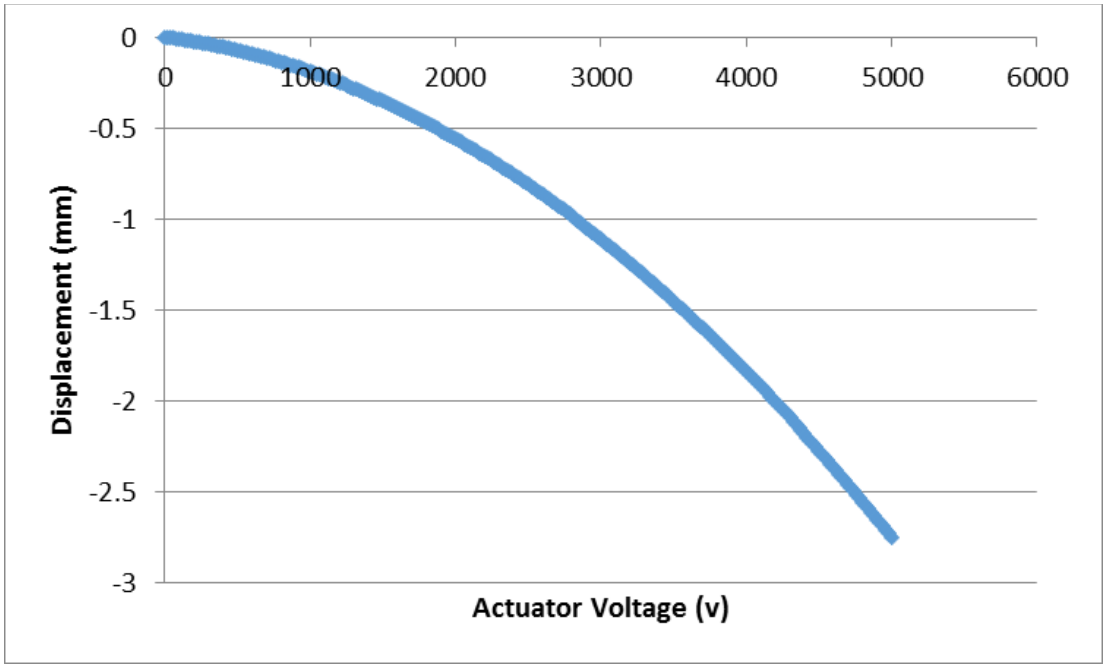

Figure B-1: Actuator voltage vs displacement curve, mechanically biased by variable modulus structure

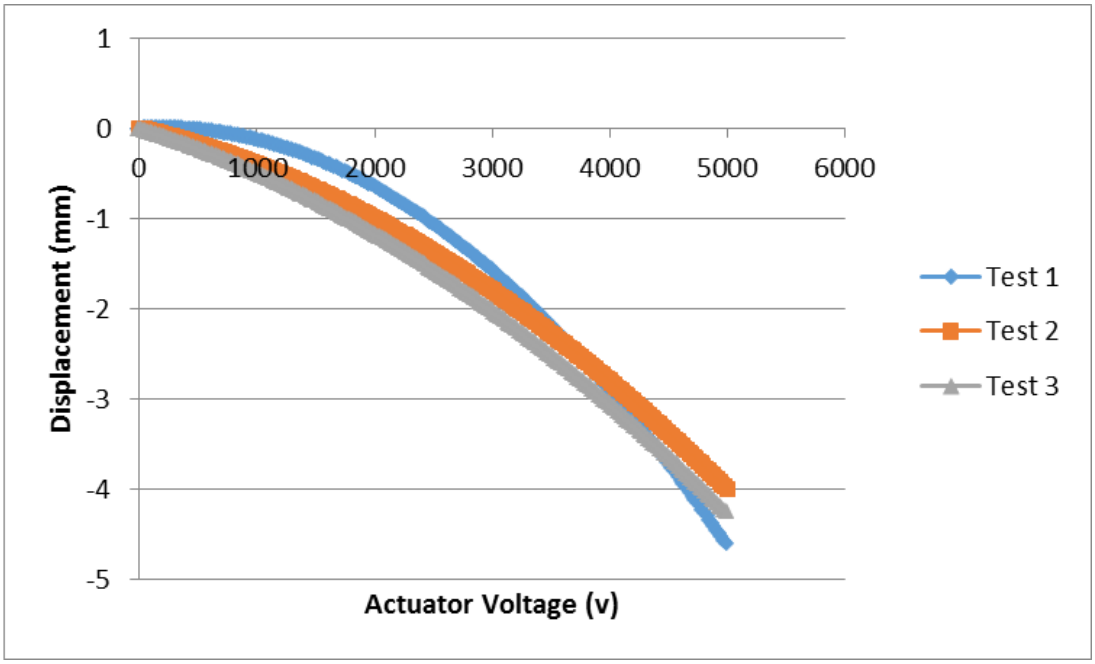

Figure B-2: Actuator voltage vs displacement curves from three successive tests, mechanically biased by variable modulus structure. Viscoelastic relaxation is apparent from test 1 to 3

BIBLIOGRAPHY

Berardi, U. (2011). "Modeling and testing of a dielectric electro-active polymer (DEAP) actuator for active vibration control." *Journal of Mechanical Science and Technology* **27(1)**.

Brown, D. (2015). "Tracker Video Analysis and Modeling Tool." from https://www.cabrillo.edu/~dbrown/tracker/.

Chiba, R. et al. (1999). "High-field electrostriction of elastomeric polymer dielectrics for actuation." *Smart Structures and Materials 1999: Electroactive Polymer Actuators and Devices, Proc. SPIE*, **3669**: 149-161.

Craig A. Steeves, K. H. T., Peter T. Maxwell, Luigi Martinelli, Richard B. Miles (2009). "Design and Manufacture of a Morphing Structure for a Shape-Adaptive Supersonic Wind Tunnel Nozzle." *Journal of Applied Mechanics* **76**.

D. DeTommasi, G. P., G.Zurlo (2012). "Taut states of dielectric elastomer membranes." *International Journal of Non-Linear Mechanics* **47**.

Daniel M. Vogt, Y.-L. P., Robert J. Wood (2013). "Design and Characterization of a Soft Multi-Axis Force Sensor Using Embedded Microfluidic Channels." *IEEE Sensors Journal* **13**(10).

Engelstad, M. et al. (2009). "Analysis of Coulomb and Johnsen-Rahbek electrostatic chuck performance in the presence of particles for EUV lithography." *Proc. SPIE 7271, Alternative Lithographic Technologies* **7271**.

Federico Carpi, G. F., Danilo De Rossi (2010). "Hydrostatically Coupled Dielectric Elastomer Actuators." *IEEE/ASME Transactions on Mechatronics* **15**(2).

Federico Carpi, R. K., Peter Sommer-Larsen, Danilo De Rossi, Gursel Alici (2011). "Guest Editorial, Introduction to the Focused Section on Electroactive Polymer Mechatronics." *IEEE/ASME Transactions on Mechatronics* **16**(1).

Gabriel Murray, F. G. (2010). "Multi-layered controllable stiffness beams for morphing: energy, actuation force, and material strain considerations." *Smart Materials and Structures* **19**.

Gianluca Rizzello, D. N., Alexander York, Stefan Seelecke (2013). "Modeling and Position Control of an Electromechanical Actuator Based on a Mass-Spring-Biased EAP System." *IEEE*.

Glenn S. Bushnell, D. A., Robert Ruggeri (2008). "Shape control of a morphing structure (rotor blade) using a shape memory alloy actuator system." *Proc. SPIE 6928, Active and Passive Smart Structures and Integrated Systems 2008*.

Gross, K. E. (2008). Mechanical characterization of shape memory polymers to assess candidacy as morphing aircraft skin. *Mechanical Engineering and Materials Science*, University of Pittsburgh.

Gutierrez-Lemini, D. (2014). *Engineering Viscoelasticity*, Springer.

J. Wissman, L. F., L. Deseri, and C. Majidi (2014). "Saddle-like deformation in a dielectric elastomer actuator embedded with liquid-phase gallium-indium electrodes." *Journal of Applied Physics* **116**(14).

Jean-Baptiste Chossat, Y.-L. P., Robert J. Wood, Vincent Duchaine (2013). "A Soft Strain Sensor Based on Ionic and Metal Liquids." *IEEE Sensors Journal* **13**(9).

Jiangshui Huang , S. S., Zhigang Suo , David R. Clarke (2013). "Maximizing the Energy Density of Dielectric Elastomer Generators Using Equi-Biaxial Loading." *Advanced Functional Materials*.

Jinsong Leng, S. D. (2010). *Shape Memory Polymers and Multifunctional Composites* CRC.

Kwangmok Jung, K. J. K., Hyouk Ryeol Choi (2008). "A self-sensing dielectric elastomer actuator." *Sensors and Actuators* **143**.

Ladd, C. (2015). Ionomer info/samples. E. George.

McTeer, S. Q. a. A. (2007). "Wafer dependence of Johnsen–Rahbek type electrostatic chuck for semiconductor processes." *Journal of Applied Physics* **102**.

Mickaël Lallart, C. R., Pisan Sukwisut, Lionel Petit, Daniel Guyomar, Nantakan Muensit (2012). "Electrostrictive bending actuators: Modeling and experimental investigation." *Sensors and Actuators A: Physical*(179): 169-177.

Naudin, J.-L. (2004). "JLN Labs, The LIFTER Project." from http://lifters.online.fr/.

Ogden, R. W. (1972). "Large Deformation Isotropic Elasticity - On the Correlation of Theory and Experiment for Incompressible Rubberlike Solids." *Proceedings of the Royal Society of London. Series A, Mathematical and Physical Sciences* **326**(1567): 565-584.

Patrick T. Mather, et al. (2009). "Shape Memory Polymer Research." *Annual Review of Materials Research* **39**(1): 445-471.

Philen, M. (2010). Tunable Modulus Structures utilizing Fluidic Flexible Matrix Composites: Analytical and Experimental Investigations. *51st AIAA/ASME/ASCE/AHS/ASC Structures, Structural Dynamics, and Materials Conference*, Orlando, Florida, American Institute of Aeronautics and Astronautics.

Philippe Dubois, S. R., Muhamed Niklaus, Massoud Dadras, Herbert Shea (2008). "Voltage Control of the Resonance Frequency of Dielectric Electroactive Polymer (DEAP) Membranes." *Journal of Microelectromechanical Systems* **17**(05).

Poole, M., Hamann, A. (2012). *Making modern living possible*. Danfoss PolyPower A/S;.

Prasanth Thummala, Z. Z., Michael A. E. Andersen, Ole C. Thomsen "A high voltage DC-DC converter driving a Dielectric Electro Active Polymer actuator for wind turbine flaps."

Rauscher, S. G. (2008). Testing and Analysis of Shape-memory Polymers for Morphing Aircraft Skin Application. *Mechanical Engineering and Materials Science*, University of Pittsburgh.

S. Timoshenko, J. N. G. (1951). *Theory of Elasticity*, McGraw-Hill.

Samuel Shian, R. M. D., David R. Clarke (2013). "Tunable lenses using transparent dielectric elastomer actuators." *Optics Express*.

Sarban, R. W. J. a. R. (2012). "Inverse grey-box model-based control of a dielectric elastomer actuator." *Smart Materials and Structures* **21**.

Shahin Zareie, A. Z., Aydin Azizi (2011). "Buckling control of morphing composite airfoil structure using multi-stable laminate by piezoelectric sensors/actuators." *Proc. SPIE 7978, Behavior and Mechanics of Multifunctional Materials and Composites*.

ShuangWang, John C. Brigham (2012). "A computational framework for the optimal design of morphing processes in locally activated smart material structures." *Smart Materials and Structures* **21**.

Sommer-Larsen, et al. (2002). "Mechanical properties of Dielectric Elastomer Actuators with smart metallic compliant electrodes." *Smart Structures and Materials 2002: Electroactive Polymer Actuators and Devices, Proc. SPIE*, **4695**: 150-157.

Stephen Daynes, A. G., Annela Seddon, Richard Trask (2013). "Morphing structures using soft polymers for active deployment." *Smart Materials and Structures* **23**.

Tevet-Deree, L. (2008). Electroactive Polymer Composites - Analysis and Simulation. *Mechanical Engineering*, Ben-Gurion University of the Negev.

Tong Lu , L. F., James Wissman , and Carmel Majidi (2014). "Rapid Prototyping for Soft-Matter Electronics." *Advanced Functional Materials* **2014**.

Wanliang Shan, T. L., Carmel Majidi (2013). "Soft-matter composites with electrically tunable elastic rigidity." *Smart Materials and Structures* **22**.

Wissler, M. T. (2014). Modeling dielectric elastomer actuators, Swiss Federal Institute Of Technology in Zurich.

Yijin Chen, J. S., Yanju Liu and Jinsong Leng (2012). "Variable stiffness property study on shape memory polymer composite tube." *Smart Materials and Structures* **21**(9).

Yong-Lae Park, R. J. W. "Smart Pneumatic Artificial Muscle Actuator with Embedded Microfluidic Sensing."